# DESIGN AND GROWTH OF ORGANIC SEMICONDUCTORS FOR ORGANIC THIN FILM TRANSISTORS

A Dissertation

Presented to the Faculty of the Graduate School

of Cornell University

In Partial Fulfillment of the Requirements for the Degree of

Doctor of Philosophy

by

Vladimir A. Pozdin

May 2011

# DESIGN AND GROWTH OF ORGANIC SEMICONDUCTORS FOR ORGANIC THIN FILM TRANSISTORS

Vladimir A. Pozdin Ph. D.

Cornell University 2011

Organic field-effect transistors are attracting much attention due to possible applications in flexible electronics, but low electronic performance and stability remain challenges to realizing such applications. Nevertheless, molecular semiconductors have already been successfully integrated in commercial products such as organic displays, luminaires, and photovoltaics. While polymeric materials have historically lagged behind, they are currently gaining significant attention due to their ease of processing, which does not require a vacuum deposition system.

Polymeric materials present a number of challenges, from designing the structure of the monomer to finding the optimum molecular weight. We present an exhaustive structure-property relationship study of a newly synthesized family of thienoacenes. Based on the results of our study, we suggest $C_2$ symmetry for the repeat unit as a new design criterion to aid in the development of future polymeric semiconductors. In addition, we investigate the thermal stability of our polymers using *ex-situ* and *in-situ* X-ray scattering. We identify an irreversible reorganization due to solution processing, as well as a reversible thermal expansion with linear expansion coefficient of $2\times10^{-4}$ $°C^{-1}$. By optimizing polymer structure and processing conditions, we have achieved a field-effect hole mobility of 0.3 $cm^2/Vs$ and

environmental stability exceeding one year.

Even though molecular electronics, such as OLEDs with AlQ3, have already been commercialized, the fundamental questions of charge transport and trapping have not been answered for these materials, owing to the high degree of anisotropy in molecular thin films. We report an unexpected reorganization of molecular thin films of pentacene on commonly used $SiO_2$ substrates treated with a self-assembled monolayer under inert conditions. In addition, we investigated the process of solvent annealing of an insoluble molecular semiconductor. The method of solvent annealing is further demonstrated as a feasible process to improve crystallinity in organic films without the adverse effects of thermal annealing.

## BIOGRAPHICAL SKETCH

Vladimir Aleksandrovich Pozdin was born in L'vov, Ukrainian Soviet Socialist Republic on September 7th, 1984. His parents were both electrical engineers specializing in lasers and were employed by the large soviet conglomerate, Polyaron. The demise of the Soviet Union brought hard times upon the family, as first Vladimir's mother was laid off and in the years to follow his father's employment started to lose its financial benefits, with wages being withheld for months at a time. In 1997 an opportunity presented itself for his father to pursue a job opportunity in small town of Hermann, MO in the heartland of America, which was impossible to refuse. After six months, Vladimir and his mother followed his father to what became their new home, America, leaving family, friends, and childhood behind. In 2001, Vladimir was accepted to the Missouri Academy for Math, Science, and Computing. It was there that he regained his passion and motivation for learning. Upon graduation, Vladimir enrolled in a dual degree program between Butler University and Purdue University in Indianapolis, double majoring in Physics and Electrical Engineering. It was at Butler University, that Vladimir met Professor Pharrell, who mentored him on number and game theory. In the end, it was Professor Han from Physics, who steered Vladimir towards physics and introduced him to nanotechnology during a summer research at University of Science and Technology of China in Hefei, China. Upon completion of a five year program in three years, Vladimir's thirst for knowledge led him to enroll in a graduate program at Cornell University, joining the group of a charismatic young scientist, George Malliaras, where he worked on the dream of amazing plastic electronics.

To my grandfather, Vladimir Aleksandrovich Pozdin.

# ACKNOWLEDGMENTS

Thanks are due to all the members of the Malliaras group for fruitful discussions, assistance, and support, members of the Ober group and in particular, Dr. Priscilla Taylor for fluorinated photoresist and cookie preparation that enabled much of the work presented, Tushar Desai, and members of the Marohn group for great collaborations and harboring. Much of this work was enabled by the Cornell High Energy Synchrotron Source (CHESS) and their amazing staff, in particular Detlef-M Smilgies and Arthur Woll. CHESS is supported by the NSF (DMR-0936384). This work was supported by a National Science Foundation (NSF) Graduate Fellowship and the Cornell Center for Materials Research of the NSF (DMR-0520404). Additional funding and support was provided by Corning Inc. A portion of this work was conducted at the Cornell NanoScale Facility, a member of the National Nanotechnology Infrastructure Network, which is supported by NSF (Grant ECS-0335765) and at the Cornell Nanobiotechnology Center's shared experimental facilities supported by the NSF (ECS-9876771). Most importantly, I would like to thank George Malliaras for his support and guidance and John Marohn for his guidance during George's absence.

TABLE OF CONTENTS

LIST OF FIGURES

LIST OF TABLES

LIST OF EQUATIONS

# CHAPTER 1

# INTRODUCTION TO ORGANIC SEMICONDUCTORS

## *Organic Electronics*

Organic electronics have been attracting the attention of scholars for over five decades now, due to their new type of electronic structure and the promise of low-cost, large-area electronics for a variety of applications, including flexible circuits, displays, and biological sensors. However, these materials failed to make a significant impact, until the applications of organic materials in organic light emitting diodes (OLEDs) [1, 2] and organic thin film transistors (OTFTs) [3, 4, 5] were demonstrated in the mid 80's. Further improvement in performance and efficiency spurred technology companies to invest in further development of organic electronics. The entire field suffered a severe setback, as the scandal with Schön shed doubt on the entire organic electronics community. But through hard work and perseverance, the scientific community was able to regain the public's trust and demonstrate the feasibility of organic electronics.

The real advantage of organic semiconductors over their inorganic counterparts is in their ease of processing. Solubility in organic solvents enables the spin casting [6, 7], inkjet printing [8, 9], or imprinting [10, 11] of these materials on a variety of substrates. Material properties are also highly tunable through chemical synthesis. In addition, the current trend in electronics away from multifunctional devices to dedicated function devices has led to many niche opportunities for organic electronics. Organics are not without their down side, the most frequently cited of which being poor electronic performance and stability. Poor electronic performance remains a

barrier to be overcome to this day, but in many cases the performance has been demonstrated to be sufficient to drive displays or for sensing applications, where the emphasis is on compatibility and low cost.

Today, organic electronics are no longer a dream, but a major component of many consumer products. The applications of organic electronics can be broadly divided into four areas: organic light emitting diodes (OLEDs), organic photovoltaics (OPVs), organic thin film transistors (OTFTs), and sensors. The relative amount of interest in these areas can be seen from the number of publications per year for each of these topics (see Figure 1.1). The most mature of these areas is OLEDs. In fact, much of the research in OLED applications of organics has moved out of the scientific community and into the commercial world shrouded in trade secrets, which explains the leveling off of the number of annual publications in the field. Organic photovoltaics - devices that convert sunlight into electric current - are currently in the transition between academia and industry, with a small number of products already available, such as the recreational-use solar panels by Konarko. Today's global demand for energy has significantly increased the interest in OPVs. The real market potential of organics is hard to gauge, as new devices and novel applications are constantly emerging and much of the development is still in the early stages, with the exception of OLEDs. For this reason, we shall have a look at the application of OLEDs and the potential market created by this new technology.

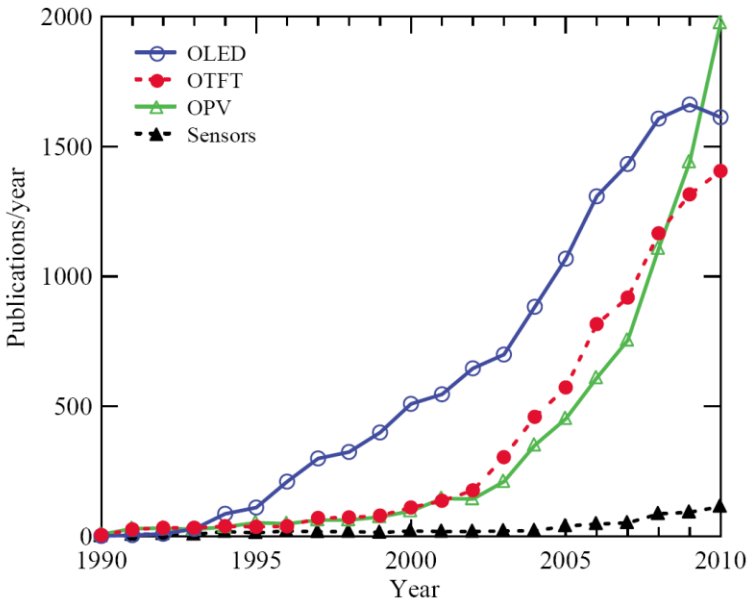


**Figure 1.1.** Number of publications per year for different areas of application for organic materials.

**OLEDs**

The lighting market for organic electronics is broken down into two sectors: luminairs, which would compete and/or complement solid state lighting, and displays. These are very different sectors, with entirely different constraints. In lighting, OLEDs offer unprecedented advantages by unlocking niche applications. With OLEDs unique ability to be transparent in the off state and semitransparent in the on state, light designers are rethinking conventional ideas of lighting. New concepts of direct lighting of museum or commercial exhibits by multifunction enclosure-luminairs have already been demonstrated and sold by OSRAM. A market report by DisplaySearch projects the increase in the OLED lighting market with the revenue exceeding $6 billion by 2018.

Organics in displays have found a number of applications, with some simply using white OLED as a backlight, while the more popular option is the Active Matrix OLEDs (AMOLED) display. These displays have a unique feature of being direct emitters, which reduces the display construction by removing the backlight, color filters, and one of the polarizers. This trimming of the construction results in a reduction of the thickness and weight of the display, which is favorable in smartphone applications. A number of challenges remain in the display market, such as reliability, scaling, and the support circuitry. Reliability has been an issue with organics, especially for blue OLEDs, but clever design by Universal Display Corp. of 4 pixel displays with deep, short lifetime blues and light, long lifetime blues allow for a way around this limitation. While there are challenges with OLED display, they have proven to be rugged enough to have passed military specifications, and mini OLED displays are currently being used in helmet mounted displays by soldiers in combat.

While one of benefits of the organics has always been the ease of processing, it has not been utilized in the display business. Most of the active materials in the commercial displays are vacuum deposited small molecules, which limits the processing size of the substrate. Currently, Veeco offers the largest linear deposition source capable of meeting the capacity for Gen VI (1.5m x 1.8m) substrates. Another issue is the driving circuitry in the displays. There is a push to create flexible drive circuits to achieve flexible and 3D displays, and a number of materials could be up to the challenge. Oxide materials offer great semi-transparency and n-type transport, but there is still a lack of a good p-type semiconductor compatible with flexible processing. That is where the development of organic thin film transistors has found a

major foothold, because organics semiconductors are typically p-type and could offer the necessary performance to drive the future flexible and 3D displays.

***Dissertation Outlook***

Organic semiconductors can be categorized into three classes: conjugated polymers, small molecules, and molecularly doped polymers. This dissertation investigates the design and optimization of new family of polymer semiconductors (Chapter 2), and growth and processing of small molecules (Chapter 3) with the goal of improving crystallinity and transport properties.

Through collaboration with Corning Inc., I investigated the relationship between polymer structure, thin film packing, and electronic transport. By identifying the structural features responsible for optimal packing and transport, I was able to suggest to my collaborators at Corning Inc. promising new structures. After an extensive study, a general trend began to emerge and we proposed the $C_2$ symmetry design criterion for polymeric semiconductors. In further investigation of thermal stability of polymer semiconductors, I identified that the optimal polymer should not undergo melting or phase transition up to 200 °C, in order to prevent unexpected changes in thin film properties. Working with polymers designed in our collaboration, I observed reorganization upon thermal annealing not apparent from typical DSC measurement.

In other work on molecular semiconductors, I investigated the growth of thin films in order to understand growth processes responsible for formation of films with optimal transport properties. In the process of studying thin films, I observed thin film reorganization under inert atmospheres and through collaboration with Professor Engstrom's group, we demonstrated the detrimental effects of comparing different *ex-situ* or *in-situ* results without careful consideration of thin film reorganization.

Borrowing from the solvent annealing work of block-copolymers in Professor Ober's group, we investigated the dynamics of solvent annealing an insoluble molecular thin film. Such solvent annealing produces films with increased roughness, which would be favorable for solar cell applications. I investigated the use of solvent annealing of a solar cell material to enhance the crystallinity, as an alternative to thermal annealing at 265 °C.

# CHAPTER 2

# DESIGN OF POLYMERIC SEMICONDUCTORS

## *1.1 Introduction to polymeric semiconductors*

The development of thin film transistors based on polymeric semiconductors is an important step for the realization of large-area, mechanically flexible electronics [7]. Initial development of thiophene was the fuctionalization of the thiophene backbone with alkane side-chains in order to achieve solubility [12, 13]. Further improvements in symmetric structure synthesis have led to the emergence of regioregular poly(3-hexylthiophene) (P3HT) as the benchmark for this class of materials with field-effect hole mobilities up to 0.1 $cm^2/Vs$ [14]. Since then, the performance of polymeric semiconductors has greatly improved with design attention shifting towards the manipulation of the conjugation length in order to achieve oxidation stability and improve self-assembly. The reduction of the number of alkyl substituents on the thiophene backbone in poly(3,3”-diakylquarterthiophene)s (PQTs) was found to promote self-assembly and crystallization, resulting in a field-effect hole mobility up to 0.2 $cm^2/Vs$ after post-deposition annealing [15]. Further incorporation of unsubstituted thiophene rings along the backbone in poly(2,5-bis(alkyl-thiophen-2-yl)thieno[3,2-b]thiophenes) (PBTTT) has led to formation of crystalline regimes, so that the polymer main chains can assemble into large domains on crystallization from liquid crystal phase. PBTTT field-effect mobilities of 0.2 – 0.6 $cm^2/Vs$ have been reported [16]. In addition, the introduction of the unsubstituted thiophene rings in PBTTT has led to reduction of the conjugation along the backbone, widening the bandgap and improving the oxidation stability of the polymer.

Current understanding of conjugated polymer design calls for a planar and rigid backbone with extended π-conjugation, which would promote self-assembly and close packing and allow efficient intermolecular charge transfer [17]. The design calls for alkyl side-chains with appropriate length to ensure solubility of the rigid and otherwise insoluble backbone. The alkyl side-chains need to be of optimal length and arranged at appropriate density to allow for solubility, while not inhibiting the self-assembly or the conjugation of the backbone. Further, the conjugation length should be controlled in order to achieve a high ionization potential (IP), or the highest occupied molecular orbital (HOMO) level, in order to improve the oxidation stability of the polymeric material.

Our collaborators at Corning Inc. have developed a method to synthesize β-alkylsubstituted fused thiophene compounds [18], which have been made soluble by addition of alkyl side-chains. The synthesis method allows for incorporation of unsubstituted thiophene rings into the fused thiophene compounds and polymerization through α-positions, resulting in a family of thienothiophene polymers. The synthesis of new family of thienothiophene in which every aspect of the polymer can be altered has led to an extensive structure-property relationship study [19, 20, 21] presented in this chapter. First, we investigate the role of the fused thiophene rings, making up the backbone [20]. Based on those results, we choose the best candidate to further study the role of the unsubstituted thiophene rings in the backbone [21]. Lastly, we investigate the role of alkyl side-chains and the effect of thermal annealing on the stability of thin films [22]. In the next section, we introduce a novel and valuable

technique to analyze structure and crystallinity of thin films using X-Rays called Grazing Incidence Wide Angle X-Ray Scattering (GIWAXS).

### *1.2 Grazing Incidence Wide Angle X-Ray Scattering*

Electronic properties of polycrystalline and semicrystalline materials are highly dependent on the material's morphology and microstructure. For this reason, there has been much effort devoted to correlating the microstructure and properties of thin films by Scanning Electron Microscopy (SEM), Transmission Electron Microscopy (TEM), Atomic Force Microscopy (AFM), and most importantly X-rays. One of the most useful techniques in studying the properties of thin film polymeric or molecular semiconductors is Grazing Incidence Wide Angle X-Ray Scattering (GIWAXS). The geometry used in GIWAXS is show in Figure 2.1. Grazing-incidence geometry limits the X-ray penetration into the substrate, as the incident angle is maintained below the critical angle of the substrate [23, 24, 25]. This enables analysis of thin films on various substrates, which is not possible in the case of transmission techniques or when the scattering from the substrate overlaps with the weaker signal from the thin film. In addition, X-ray penetration depth may be varied depending on the incident angle in order to analyze the variation in microstructure of thin film over its thickness. One of the issues with organic semiconductors is their weak scattering, due to low crystallinity, low crystal symmetry, and small scattering cross section. The high photon flux of synchrotron radiation and large beam footprint across the sample at grazing incidence allow for efficient diffraction measurements with organic thin films. Fast collection of scattering intensities with a 2-D detector in both out-of-plane and in-plane directions avoids radiation damage to the thin films and makes GIWAXS the idea tool for *in-situ* and *ex-situ* measurement of organic semiconductor microstructure.

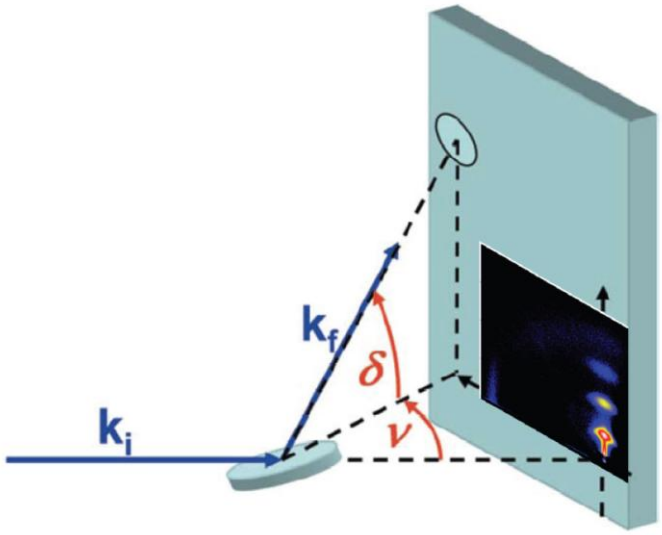


**Figure 2.1.** Scattering geometry and typical polymer diffraction pattern for GIWAXS.[26]

Typically, polymer semiconductors form lamellar films as shown in Figure 2.2, with the rigid backbone aligning parallel to the substrate. In this case, the typical 2-D scattering intensity collected from thin films, shown in Figure 2.3, has two characteristic features. One of those features is the diffuse scattering in the out-of-plane direction corresponding to the lamellar spacing and the other is the in-plane reflection corresponding to the π-π stacking distance or the interchain separation. In addition to the characteristic stacking distances, we can calculate the correlated lamellar thickness [24] and mosaicity of the lamellar stacks. The mosaicity is determined from the Full Width at Half Maximum (FWHM) of the diffuse lamellar scattering peaks and indicates the average misorientation of crystalline domains in the thin film (see Figure 2.3). Therein, lower mosaicity indicates better alignment of crystalline domains in the film.

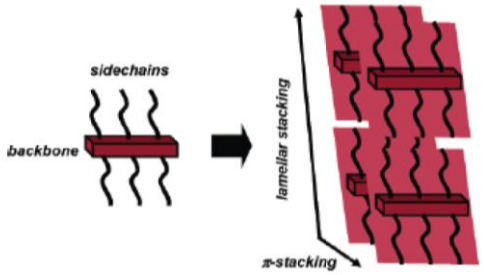


**Figure 2.2.** Typical lamellar stacking of polymers [27], characterized by the out-of-plane stacking distance, lamellar spacing, and the in-plane stacking distance, π-π spacing.

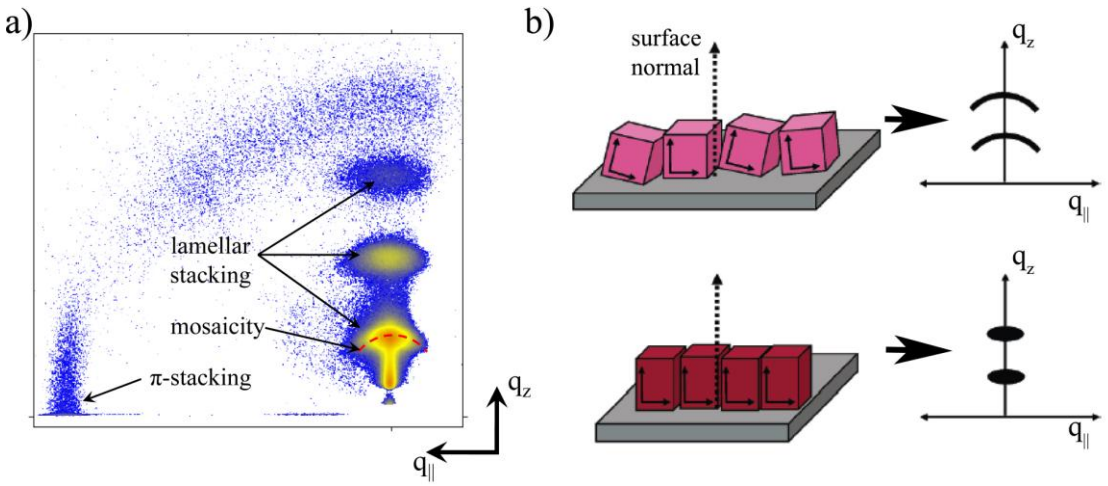


**Figure 2.3.** (a) Typical polymer diffraction pattern for GIWAXS showing the diffuse lamellae peaks and the in-plane π-π stacking peak. Mosaicity is determined by the FWHM of the (001) peak radial distribution, as shown. (b) Misaligned crystalline domains in thin film cause radial broadening of the (001) peak, where as highly aligned domains result in a sharply defined narrow peak [27].

### *2. Role of Backbone in Packing*

The rigid backbone of the investigated family of thienothiophenes is made up of two separate components: fused thiophene rings and unsubstituted thiophene rings. Fused thiophene rings are very rigid and represent the conjugated unit of the monomer, which should strongly affect the bandgap and the ionization potential of the polymer. The unsubstituted thiophene rings have some flexibility compared to the rigid fused component, which allows them to rotate out of the plane of the rigid backbone to reduce steric hindrance in thin film. Additionally, unsubstituted thiophene rings serve to break up the conjugation along the polymer backbone to further affect the bandgap and ionization potential. In the following sections we analyze the effect of the two backbone components on thin film properties and electronic transport.

### *2.1 Role of Fused Thiophene Component*

#### *2.1.1 Experimental*

Three polymers, namely, poly(2,5-bis(thiophene-2-yl)-(3,5-didecanyltrithienoacene) (P2TDC10FT3), poly(2,5-bis(thiophene-2-yl)-(3,7-didecanyltetrathienoacene) (P2TDC10FT4), poly(2,5-bis(thiophene-2-yl)-(3,6-didecanylpentathienoacene) (P2TDC10FT5) were synthesized using published procedures [20]. The structure and molecular weights of the polymers are summarized in Figure 2.4. Polymer molecular weight is important, because it determines many physicals properties, including transition temperatures and mechanical properties. The most commonly used value is the number average molecular weight, *Mn*, which is only sensitive to the number of molecules present. For polymer properties that depend on the weight and not size of the polymer chains, the weight average molecular weight, *Mw*, is more insightful. Ideal polymers are monodispersed and contain the

same number of monomers in each chain, but that is not always the case. Polydispersity index, *PDI*, is *Mw/Mn* and is a measure of the distribution width of molecular mass in a polymer.

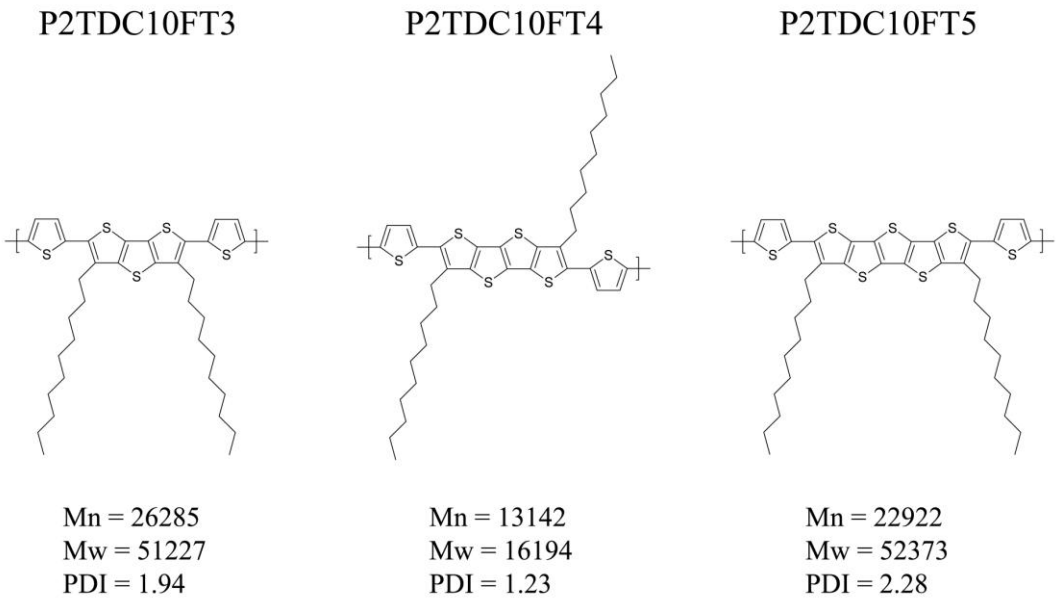


**Figure 2.4.** Structure and polydispersity index (PDI) of P2TDC10FT3, P2TDC10FT4, and P2TDC10FT5.

Solutions of polymers in pentachloroethane at concentrations of 3 mg/mL were prepared by heating to 170°C for 30 min with stirring to speed up dissolution. Silicon oxide substrates were cleaned by sonication in semiconductor grade acetone and isopropanol for 10 min in each solvent, and then given a 15 min air plasma treatment. Polymer thin films were then deposited by spin-casting at 1500 rpm for 40 s. The films were the baked at 150°C in a vacuum chamber.

GIWAXS was performed on the samples at the D1 station of the Cornell High Energy Synchrotron Source (CHESS). A wide bandpass (1.5%) double-bounce multilayer monochromator defined a 10.0 keV photon beam. Samples were studied under various incident angles ranging from above the critical angle of the thin film to

slightly above the critical angle of the silicon oxide substrate. This was done in order to optimize the scattering from the thin film with minimal substrate reflections. Scattering intensities were recorded using a 2-D area detector (MedOptics). Working sample to detector distances were 89, 88, and 91 mm for P2TDC10FT3, P2TDC10FT4, and P2TDC10FT5, respectively. Scattering vectors were calculated [24] and refraction corrected [28, 23].

With a dielectric substrate, there are two possible configurations for field-effect transistors: top contact and bottom contact, as shown in Figure 2.5. Typically, organic materials exhibit different configuration when deposited on top of a metal, as compared to a dielectric surface. Therefore, bottom contact field-effect transistors result in reduced performance due to large series resistance, increased trapping at the grain boundaries along the electrodes, and the degraded performance in the section of the channel which has an inferior growth pattern [29]. In addition, technical difficulties arise in characterizing organic thin film with non-planar electrodes using surface scanning techniques, such as AFM, and additional scattering from metal electrodes and different organic configurations are all convoluted in X-ray scattering. For these reasons, we limit our fabrication to top contact bottom-gate transistors.

Top contact bottom-gate transistors using P2TDC10FT3, P2TDC10FT4, and P2TDC10FT5 as the organic semiconducting channel were fabricated in ambient conditions. Heavily phosphorus doped Si <1 0 0> wafers were used as gate electrodes with a 300nm thermally grown silicon dioxide layer as the gate dielectric. Schematic of the fabricated thin film transistors is shown in Figure 2.5. These devices operate in the accumulation regime because an accumulation of carriers builds up at the organic/dielectric interface when a negative gate bias is applied to p-type device. Under a drain-to-source voltage ($V_{DS}$), the current ($I_{DS}$) is obtained and modulated by the gate voltage ($V_{GS}$). For OTFTs, the dielectric surface is frequently treated with a

self-assembled monolayer (SAM) in order to remove hydroxyl or other polar groups at the dielectric interface that cause charge trapping [30, 29] or dope the organic channel [31, 32]. In this work, $SiO_2$ surface was treated with hexamethyldisilazane (HMDS) and octyltrichlorosilane (OTS) prior to polymer deposition. Gold top contacts (50nm) for source and drain electrodes were vacuum-deposited at a rate of 2.5 Å/s through a contact shadow mask that defined a series of transistor devices with channel length ($L$) of 80μm and a channel width ($W$) of 1mm. Polymeric transistors were characterized in vacuum using a LakeShore probe station and Keithley 2400 and 6430 SourceMeters. For current-voltage curves and transfer curves, the $V_{GS}$ was scanned from +20 to −80 V. The mobility ($\mu_i$) was evaluated from the saturation regime with $V_{DS}$ = − 80V using the following equation [33]:

$$I_{DS,sat} = \frac{W}{2L}\mu_i C_r (V_{GS} - V_{TH})^2 \qquad (1)$$

where $C_r$ is the capacitance per unit area of the gate dielectric layer, and $V_{TH}$ is the threshold voltage. $V_{TH}$ was determined from the intercept in the plot of $(I_{DS})^{1/2}$ vs $V_{GS}$.

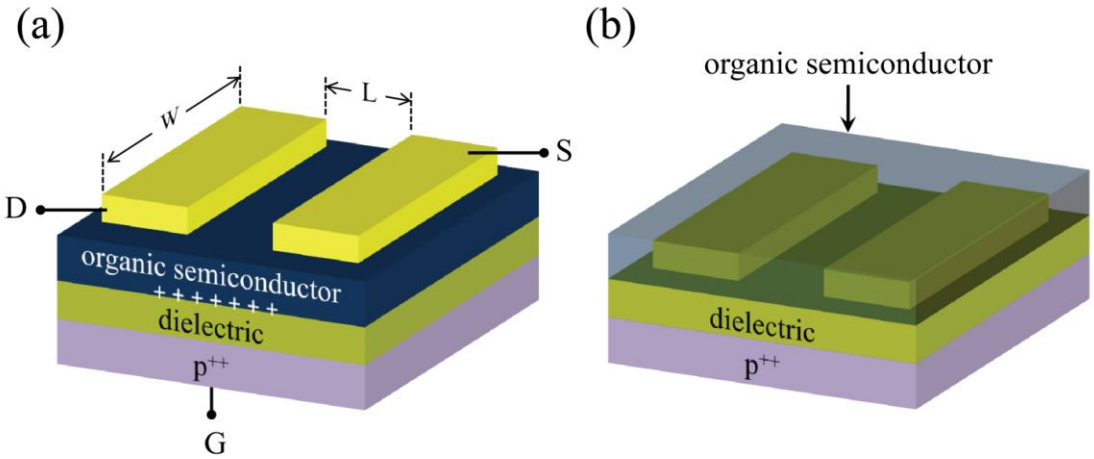


**Figure 2.5.** (a) Top contact and bottom contact (b) organic thin film field-effect transistor configurations.

### *2.1.2. Results and Discussion*

**UV-Vis.** Thin film optical absorption studies were conducted on polymer films cast from chlorobenzene solution on quartz glass to determine the conjugation of the polymers, which forms the π and π* orbitals and transport charge in organic materials. Results are shown in Figure 2.6. The absorption maxima for P2TDC10FT3, P2TDC10FT4, and P2TDC10FT5 thin films are 534, 545, and 523 nm, respectively. The maximum absorption is most red shifted in the case of P2TDC10FT4, as compared to the other two polymers, which suggests a slightly better conjugation in P2TDC10FT4. In addition, the presence of the second absorption peak in the case of P2TDC10FT4 at 583nm indicates interchain ordering, which is absent in P2TDC10FT3 and P2TDC10FT5. Such absorption data is counter intuitive, as one would expect the conjugation to increase with the length of the fused thiophene component. We speculate that the reason P2TDC10FT4 shows improved conjugation is due to the polymer packing in the thin film, which we investigate using GIWAXS.

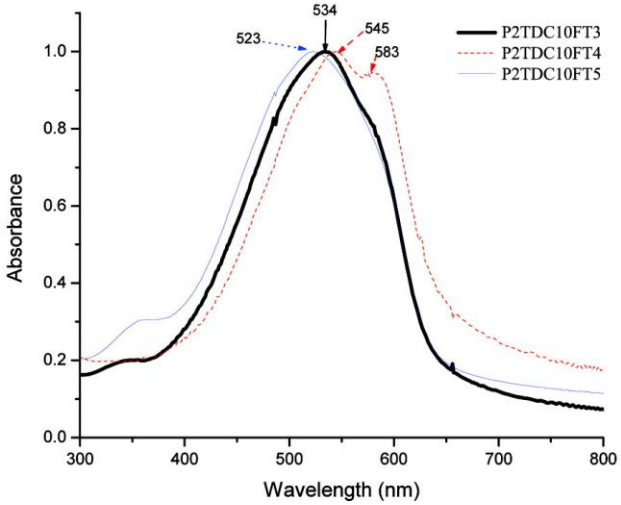


**Figure 2.6.** UV-Vis absorption of P2TDC10FT3, P2TDC10FT4, and P2TDC10FT5 thin films on quartz.

**GIWAXS.** Acquired 2-D GIWAXS patterns of polymer thin films on silicon dioxide wafers are shown in Figure 2.7, while Figure 2.8 shows the extracted scattering intensities along the $q_z$ and $q_{||}$ directions. Scattering intensities along $q_z$ and $q_{||}$ directions were obtained by radial integration as shown in Figure 2.7 (a). In addition, the background was fitted and subtracted from the scattering intensities.

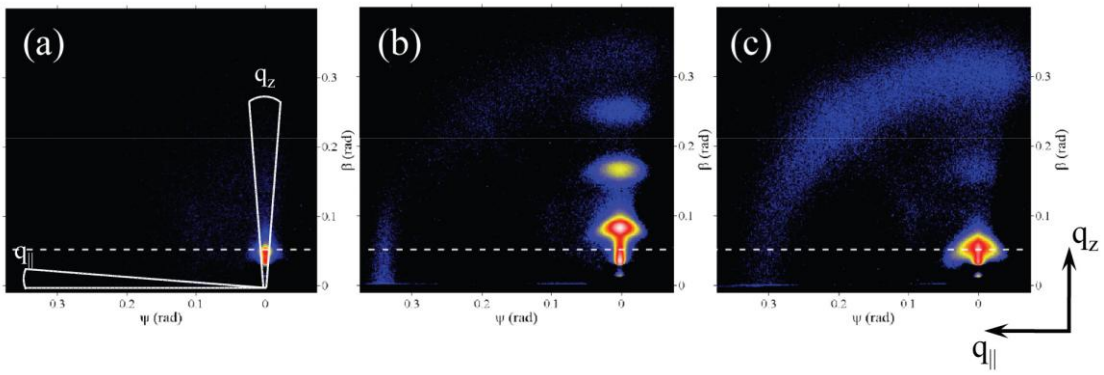


**Figure 2.7.** 2-D GIWAXS patterns of (a) P2TDC10FT3, (b) P2TDC10FT4, and (c) P2TDC10FT5 thin films. The dashed line marks the first order lamellar reflections of P2TDC10FT5, and highlights the similarity to P2TDC10FT3 and the significant difference to the P2TDC10FT4 lamellar spacing. $\beta$ and $\psi$ are scattering angles in the sample reference frame.

The scattering images from the three samples are consistent with the formation of lamellae parallel to the substrate in all cases. The most surprising difference between P2TDC10FT4 on one hand and P2TDC10FT3 and P2TDC10FT5 on the other is the significant difference in the lamellar spacing. Lamellar spacing was calculated to be 24.8, 15.0, and 22.8 Å for P2TDC10FT3, P2TDC10FT4, and P2TDC10FT5, respectively. The lamellar spacing for P2TDC10FT4 is even smaller than in P3HT (16 Å), leaving very little space for the decyl side-chains. This finding seems to be consistent with the side-chains pointing out-of-plane, which is consistent

with some other recent results in PBTTT [34]. In PBTTT, the backbone and the side-chains were rotated out of the main plane given by the monomer repeat and lamellar distance, while the molecules as a whole remained planar. Other experimental and theoretical studies concluded for P3HT, PQT, and PBTTT that the backbone planes and the side-chains are titled off the main plane [34, 35, 36, 37]. The main difference between the three investigated polymers is that P2TDC10FT3 and P2TDC10FT5 have two side-chains on the same side of the fused thiophene component, which apparently demands a different packing, as compared to P2TDC10FT4, which has side-chains on opposite sides of the fused backbone component.

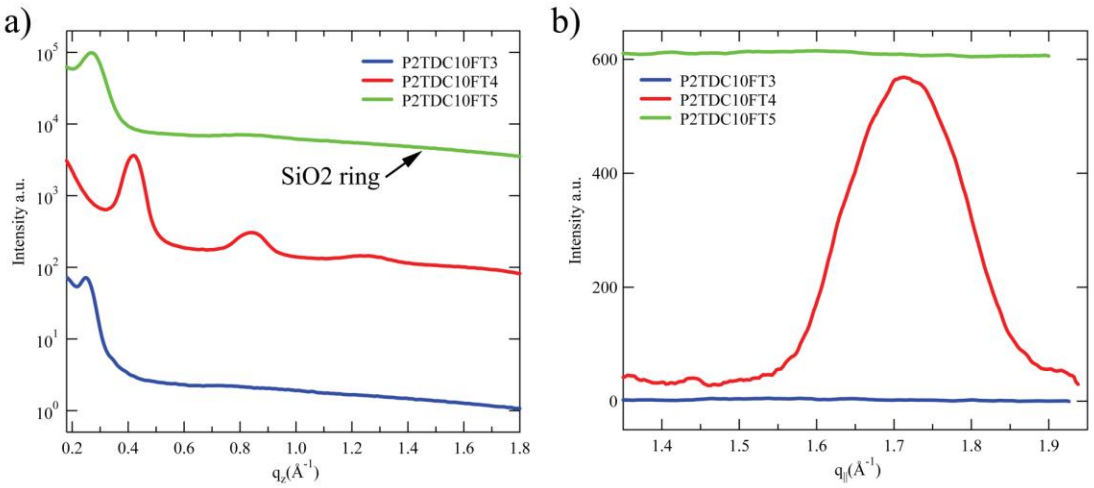


**Figure 2.8.** Scattering intensities along $q_z$(a) and $q_{||}$(b) for P2TDC10FT3, P2TDC10FT4, and P2TDC10FT5 thin films.

In Figure 2.9, we present a possible side-chain arrangement that can explain the observed lamellar spacings. For P2TDC10FT3 and P2TDC10FT5, there appears to be at best small out-of-plane tilt angle. The arrangement of the side-chains was chosen to reflect the tendency of alkanes to form a dense packing. Such packing must

have a high degree of disorder considering the observed X-ray scattering. In contrast, P2TDC10FT4 appears to behave similarly to PBTTT in its packing.

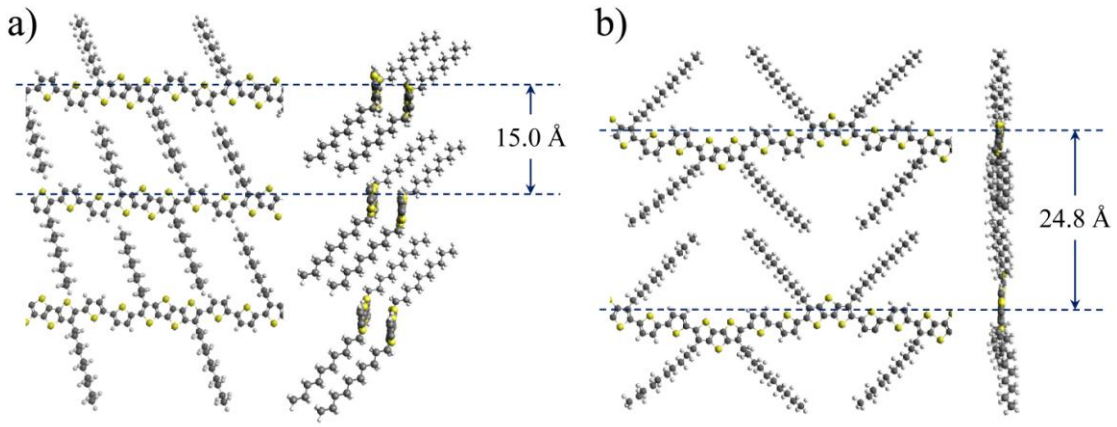


**Figure 2.9.** Proposed stacking for even-number (a) and odd-numbered (b) thienoacenes.

As seen from Figure 2.8, there are no peaks along the $q_{||}$ direction for P2TDC10FT3 and P2TDC10FT5, indicating poor in-plane ordering. The in-plane peak is observed for P2TDC10FT4 at 3.65Å, which corresponds to the π-π stacking distance. Good π-π overlap between polymer chains is crucial for electronic transport and is comparable to values obtained for PQT (3.7 Å) [15] and PBTTT (3.67-3.71 Å) [27].

**Transistor characterization.** Ultimately our aim is to correlate thin film properties to electrical transport, so in Figures 2.10 we present typical current-voltage characteristics of polymeric field-effect transistors. The output curves (Figure 2.10) show a linear behavior in the low $V_{DS}$ regime, indicating that gold electrodes form an ohmic contact with the polymers. Hole mobilities in the saturation regime, threshold voltages, and on/off ratios for P2TDC10FT3, P2TDC10FT4, and P2TDC10FT5 with various surface treatments are summarized in Table 2.1.

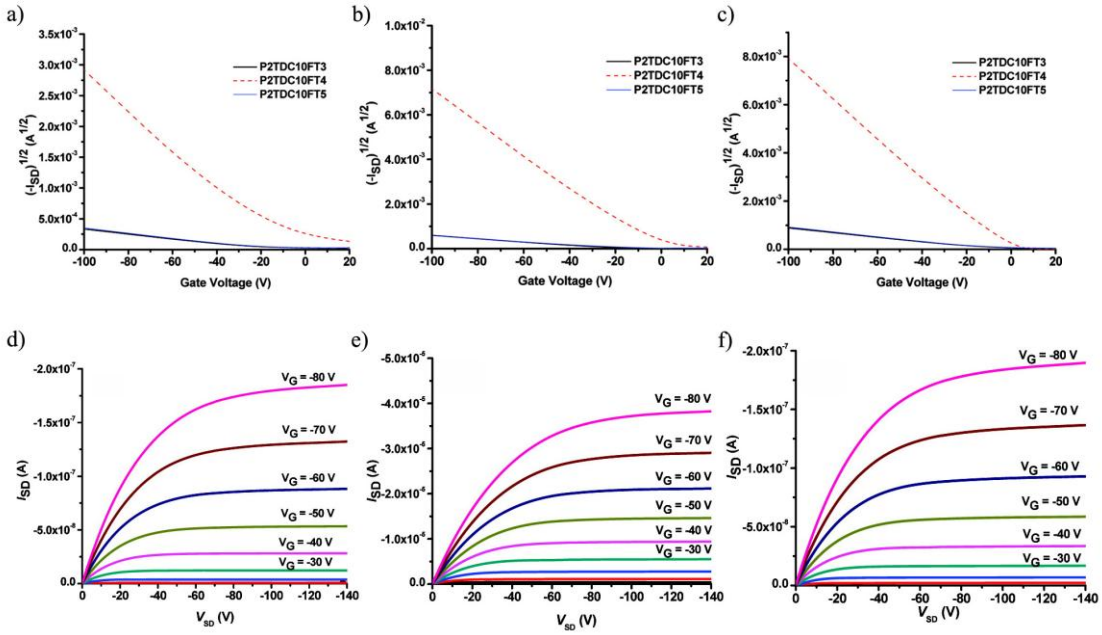


**Figure 2.10.** Transfer curves for P2TDC10FT3, P2TDC10FT4, and P2TDC10FT5 thin film transistors on bare $SiO_2$ (a), on OTS treated $SiO_2$ (b), and on HMDS treated $SiO_2$(c). Output curves for polymer devices on OTS treated $SiO_2$ for P2TDC10FT3 (d), P2TDC10FT4 (e), and P2TDC10FT5 (f).

Based on our X-ray and absorption results, it is not surprising that P2TDC10FT4 has the highest mobility among the three polymers. The polymers with three and five fused thiophenes in the backbone showed one or two orders of magnitude lower mobility values than the analogous polymer with four fused thiophene rings, which can be attributed to poor lamellar ordering as revealed by GIWAXS data. In addition, we observe a significant improvement in the field-effect hole mobility on the treated silicon dioxide substrates for all three polymers. This indicates that such surface modifications decrease the trap sites at the dielectric

interface and improve the molecular chain packing ordering of the polymer semiconductor at the dielectric/polymer interface.

**Table 2.1.** Summary of transistor performance of P2TDC10FT3, P2TDC10FT4, and P2TDC10FT5 polymer on various substrates.

| polymer | surface | average $\mu_h$ ($cm^2/Vs$) | on/off ratio | $V_{TH}$ (V) |
|---|---|---|---|---|
| P2TDC10FT3 | $SiO_2$ | 0.00011 | $10^2$ | -13 |
| | OTS | 0.00050 | $10^3$ - $10^4$ | -10 |
| | HMDS | 0.001 | $10^3$ | -11 |
| P2TDC10FT4 | $SiO_2$ | 0.010 | $10^3$ | -10 |
| | OTS | 0.065 | $10^4$ - $10^5$ | -4 |
| | HMDS | 0.072 | $10^6$ | -4 |
| P2TDC10FT5 | $SiO_2$ | 0.00015 | $10^2$ - $10^3$ | -12 |
| | OTS | 0.00055 | $10^3$ - $10^4$ | -11 |
| | HMDS | 0.0015 | $10^3$ - $10^4$ | -9 |

### *2.1.3 Conclusion*

We investigated the role of the fused thiophenes in the polymer backbone by analyzing the structure and electronic properties of P2TDC10FT3, P2TDC10FT4, and P2TDC10FT5, which have increasing number of the fused thiophenes. Absorption data revealed that all of these polymers have their conjugated units well-extended through their polymer backbone, but there was no systematic increase in the conjugation length with increasing number of fused thiophenes. This observation can be explained by the polymer ordering in the thin films, which was analyzed using GIWAXS. P2TDC10FT4 revealed a tight lamellar packing due to proper side-chain arrangement, while P2TDC10FT3 and P2TDC10FT5 packed much loosely due the steric hindrance created by the side-chain configuration. Comparing P2TDC10FT3

and P2TDC10FT5 we observed that the latter had smaller lamellar spacing and slightly improved electronic transport properties, due to the longer backbone which would serve to decrease the steric hindrance.

### *2.2. Role of Unsubstituted Component*

In the previous section we learned that four fused thiophenes in the polymer backbone resulted in a tighter lamellar packing and improved electronic transport, as compared to the odd number of fused thiophenes. We continue the structure-property investigation by fixing the number of fused thiophenes to four and varying the number of unsubstituted thiophenes from one to three.

#### *2.2.1 Experimental*

Three polymers, namely, poly(α-thienyl)-(3,7-ditri-decanyltetrathienoacene) (P1TDC13FT4), poly(2,5-bis(thiophene-2-yl)-(3,7-ditri-decanyltetrathienoacene) (P2TDC13FT4) and poly(α-terthienyl)-(3,7-ditri-decanyltetrathienoacene) (P3TDC13FT4) were synthesized using previously published procedures[19, 21]. The structure and molecular weights of the polymers are summarized in Figure 2.11.

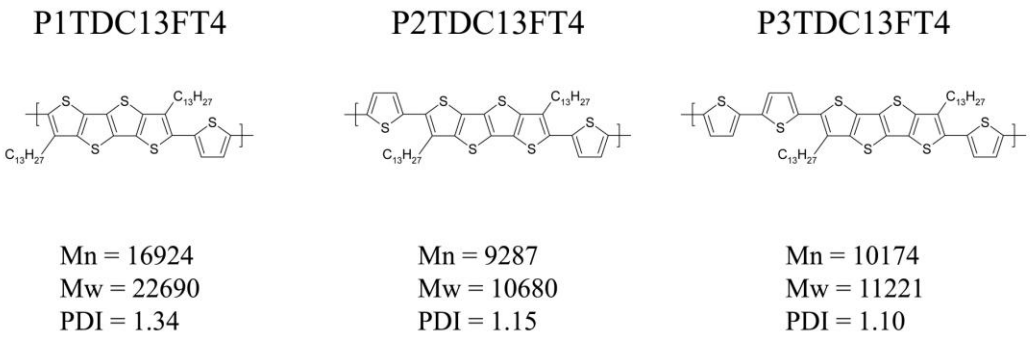


**Figure 2.11.** Structure and polydispersity index (PDI) of P1TDC13FT4, P2TDC13FT4, and P3TDC13FT4.

Solutions of polymers in pentachloroethane at concentrations of 3 mg/mL were prepared by heating to 170°C for 30 min with stirring to speed up dissolution. Silicon oxide substrates were cleaned by sonication in semiconductor grade acetone and isopropanol for 10 min in each solvent, and then given a 15 min air plasma treatment. Polymer thin films were then deposited by spin-casting at 1500 rpm for 40 s. The films were the baked at 150 °C in a vacuum chamber.

Structure and crystallinity of polymer thin films were analyzed using X-ray diffraction (XRD) with a Scintag diffractometer, employing a Cu target ($\lambda$ = 1.5405 Å). A $\theta$-$2\theta$ scan with a step size of 0.02° was set up between 2° and 12°, with scan rate of 0.02 °/s. For X-ray measurements, polymers were spin-cast on HMDS-treated $SiO_2$. These samples were further annealed at 150 °C for 10 min. Topography of the thin films was studied using Atomic Force Microscopy (AFM) in tapping mode on a Digital Instruments Model DI-3100 apparatus using Olympus OTESPA cantilevers.

Top contact bottom-gate transistors using P1TDC13FT4, P2TDC13FT4, and P3TDC13FT4 as the organic semiconducting channel were fabricated in ambient conditions according to the procedure outlined in the previous experimental section.

### *2.2.2 Results and Discussion*

***UV-Vis.*** Thin film absorption studies were conducted on polymer films cast from chloroform solution on a quartz glass. Results are shown in Figure 2.12. The absorption maxima for all three polymer thin films is 545 nm. These polymer thin films also have a second absorption peak at 589 nm for P1TDC13FT4 and P3TDC13FT4 films and 575 nm for P2TDC13FT4. A second absorption peak is indicative of interchain ordering and the red shift of this peak in the case of P1TDC13FT4 and P3TDC13FT4 indicates slightly better conjugation than in P2TDC13FT4 films. The improvement in the interchain ordering could be attributed

to improved overlap between the π-orbitals of the stacked backbones, which would be strongly affected by the backbone tilt. In the previous study, we have observed that different lamellar packing results in different backbone tilts.

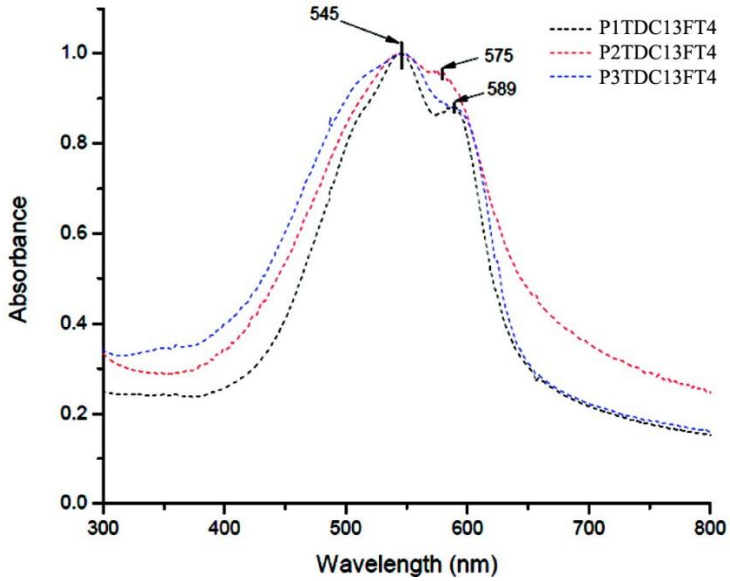


**Figure 2.12.** UV-Vis of P1TDC13FT3, P2TDC13FT4, and P3TDC13FT4 thin films on quartz. The absorption maxima is the same for the three polymers indicating similar conjugation length, regardless of the number of unsubstituted thiophene units along the backbone. All three polymers also show the second absorption peak, indicating interchain ordering.

***Structure characterization.*** In analyzing the diffraction patterns, we assume the previously observed lamella formation parallel to the substrate. From the collected diffraction patterns (Figure 2.13), we observe that the lamellar spacing varies between samples. The lamellar spacings were calculated to be 19.4, 18.7, and 24.5 Å for P1TDC13FT4, P2TDC13FT4, and P3TDC13FT4, respectively. Lamellar spacing of P3TDC13FT4 is the largest in this series of polymers, suggesting that due to the alignment of thiophene rings mediated by the strong surfur-sulfur repulsion between

the rings, the second nearest neighbor alkyl side-chains located on adjacent monomers point in the same direction. This orientation would result in much steric hindrance between the side-chains and would act to inhibit tight packing, similar to the case of the previously studied P2TDC10FT3 and P2TDC10FT5.

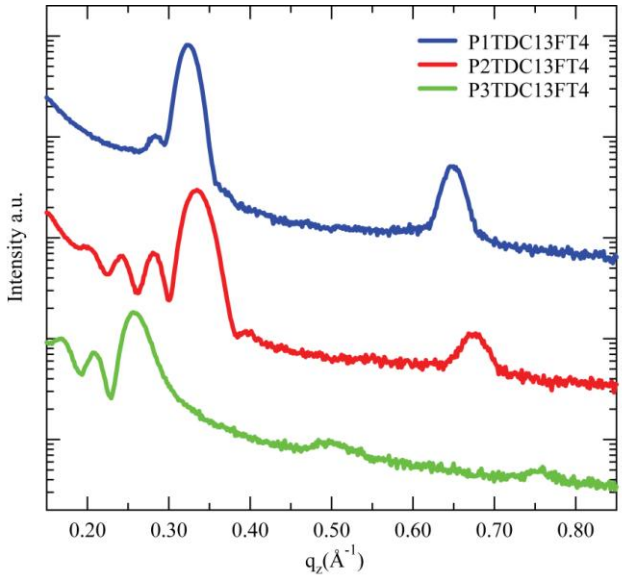


**Figure 2.13.** XRD patterns of P1TDC13FT3, P2TDC13FT4, and P3TDC13FT4. Laue oscillations for P2TDC13FT4 and P3TDC13FT4 indicate formation of highly ordered lamellae. In the case of P3TDC13FT4, lamellar spacing is observed to be significantly larger, as compared to the other two polymers.

P1TDC13FT4 has lamellar spacing similar to P2TDC13FT4, which may seem unexpected given the previous explanation for poor packing for P3TDC13FT4. This can be explained by considering the implication of a single unsubstituted thiophene ring between the fused thiophene backbones, which has an increased freedom of rotation around the single bonds between to the fused backbones, as well as increased steric hindrance due to reduced spacing between neighboring alkyl side-chains on adjacent monomers. It may be energetically favorable for the unsubstituted thiophene

ring to rotate out of the plane of the fused thiophene ring to reduce the increased hindrance of side-chains pointing in the same direction, thereby resulting in side-chains pointing in opposite directions and allowing close packing similar to P2TDC13FT4.

Using Scherrer analysis, we calculated the lamellar stack heights to be 11.4, 9.0, and 7.2 lamellae for P1TDC13FT4, P2TDC13FT4, and P3TDC13FT4, respectively. This result confirms that P3TDC13FT4 film has the worst lamellar correlation, while P1TDC13FT4 and P2TDC13FT4 have improved ordering. Additional features of the XRD measurements are the Laue oscillations close to the (001) peak in P2TDC13FT4 and P3TDC13FT4, which arise from a finite number of lamellae in the film. These oscillations suggest higher film ordering in the case of P2TDC13FT4 and P3TDC13FT4, as compared to P1TDC13FT4, where only one oscillation can be seen. The Laue oscillations yield an alternative approach to determining the lamellar stack height. From the oscillations, we are able to calculate the lamellae stack height to be 8.5 and 5.8 lamellae for P2TDC13FT4 and P3TDC13FT4, respectively, which are similar to the results from Scherrer analysis. The Laue oscillations are a direct measure of the average stack height variation, hence, P2TDC13FT4 and P3TDC13FT4 films seem to consist of a very narrowly determined distribution of lamellae, while in P1TDC13FT4, the number of lamellae in the film has a wider distribution.

The topography of the polymer films was studied using AFM and collected images are shown in Figure 2.14. In the case of P2TDC13FT4 and P3TDC13FT4, where more ordered lamellae are expected based on XRD analysis, the topography reveals a terraced lamellae, similar to PBTTT [38]. In contrast, P1TDC13FT4 has a much rougher topography and seems almost amorphous with no discernable lamellar terraces. The average terrace diameters in the P2TDC13FT4 film is significantly

higher than that for P3TDC13FT4, producing smoother films, which would be favorable to lateral charge transport. Based on XRD and AFM results, P2TDC13FT4 thin films have a small lamellar spacing and well ordered lamellae, as compared to the other two polymers. Thin films of P3TDC13FT4 create well ordered lamellar, but the lamellar stacking due to the side-chain orientation is significantly larger than P2TDC13FT4. On the other hand, the lamellar stacking in P1TDC13FT4 is comparable to P2TDC13FT4, possibly attributed to the rotation of a single unsubstituted thiophene ring out of the plane of the rigid backbone in order to achieve favorable side-chain alignment. This would produce significant steric hindrance along the in-plane direction and inhibit formation of well ordered lamellae.

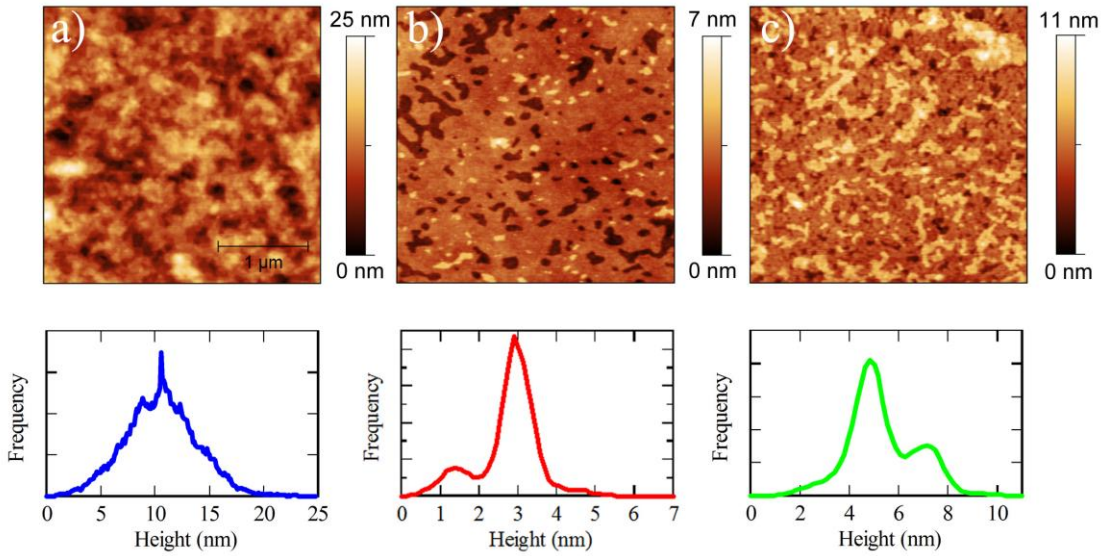


**Figure 2.14.** AFM patterns and corresponding height histograms of P1TDC13FT4 (a), P2TDC13FT4 (b), and P3TDC13FT4(c) thin films. P2TDC13FT4 and P3TDC13FT4 show clear lamellar structures with terraces, as further confirmed by the narrow height distribution with distinct peaks corresponding to exposed terraces. P1TDC13FT4 films have much rougher surface.

***Transistor characterization.*** The field-effect hole mobilities, on/off ratios, and threshold voltages for transistors fabricated on HMDS-treated surface for P1TDC13FT4, P2TDC13FT4, and P3TDC13FT4 are summarized in Table 2.2. P1TDC13FT4 with small lamellar spacing has nearly twice the mobility of P3TDC13FT4, which has large lamellar spacing but better lamellar ordering. At the same time, P2TDC13FT4 has nearly 6 times higher mobility than P1TDC13FT4 and demonstrates both smaller lamellar spacing and good lamellae ordering, attributing to its superior transport properties. It should also be noted that based on the absorption studies, P1TDC13FT4 and P3TDC13FT4 showed improved interchain interaction compared to P2TDC13FT4, but this was not sufficient for good electronic transport. Such observation can be explained by hopping transport in polymeric materials, where conjugation determines the size of the localized state, but the packing determines the spacing between these states and their coherence.

**Table 2.2.** Summary of transistor performance of P1TDC13FT4, P2TDC13FT4, and P3TDC13FT4 polymers on HMDS treated $SiO_2$. Positive $V_{TH}$ for P1TDC13FT4 and P3TDC13FT4 is attributed to charge accumulation at the dielectric interface.

| polymer | average $\mu_h$ ($cm^2/Vs$) | on/off ratio | $V_{TH}$ (V) |
|---|---|---|---|
| P1TDC13FT4 | 0.0421 | $10^3$ - $10^4$ | 10 |
| P2TDC13FT4 | 0.33 | $10^5$ | −10 |
| P3TDC13FT4 | 0.0226 | $10^4$ - $10^5$ | 5 |

### *2.2.3 Conclusion*

We investigated the role of the unsubstituted thiophene rings in the polymer backbone by analyzing the structure and electronic properties of P1TDC13FT4, P2TDC13FT4, and P3TDC13FT4, which have an increasing number of the

unsubstituted thiophenes. The results show the necessity for both close-packed structure and well ordered structure for improved electronic transport in polymer films. In addition, we observed that the effect of structure on transport is more important than the conjugation.

### *2.3 $C_2$ Design Criterion*

Based on the previous two studies of the role of backbone components on structure and transport properties, we find a strong correlation between structure and transport properties. In the first study, we varied the length of the fused thiophene component, which is expected to extend the conjugation length, but we found no evidence to support this. In addition, the transport properties were correlated with smaller lamellar packing due to side-chain arrangements along the backbone. Further investigation of the unsubstituted thiophene component demonstrated the importance of both smaller lamellar packing and better ordering to achieve the highest field-effect mobility. The correlation between the improved thin film lamellar formation and polymer structure can be explained by the symmetry of the repeat unit, shown in Figure 2.15.

Upon spin-casting, the polymer backbones arrange parallel to the substrate, with side-chains pointing normal to the substrate. This process is, to first order, random, and will lead to a distribution of orientation of the side-chains with respect to the substrate. The symmetry of the polymer repeat unit will determine the number of distinct orientations of the side-chains. In the case of both side-chains being on the same side of the backbone (Figure 2.15 $a_1$), two distinct orientations are possible: one with side-chains pointing toward the substrate and the other with side-chains pointing away from the substrate. Similarly, an asymmetric repeat unit (Figure 2.15 $a_2$), in our case due to the number of unsubstituted thiophene rings, would also yield two distinct

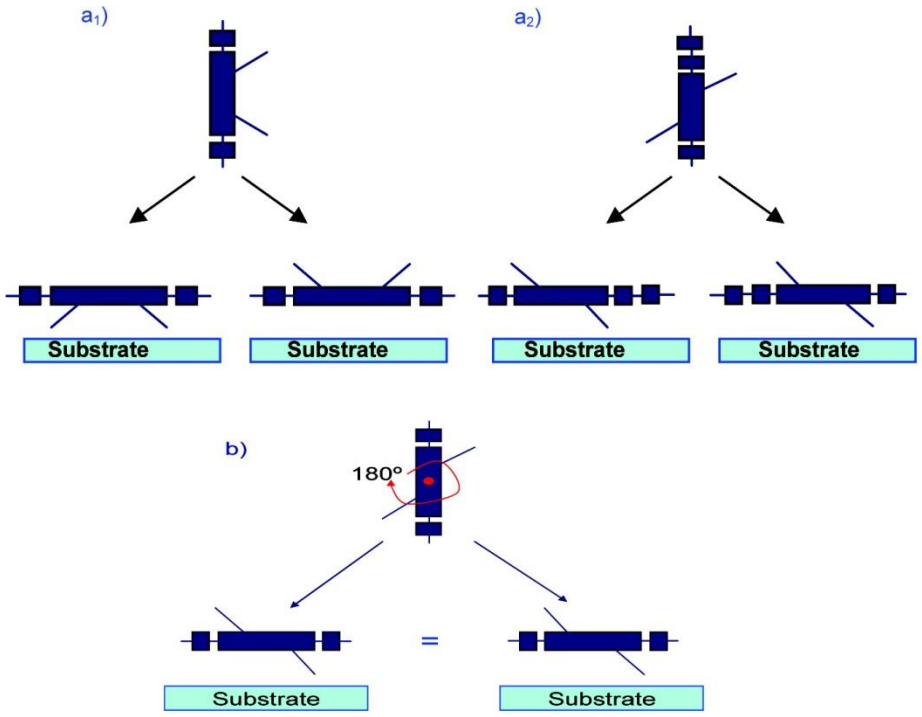


**Figure 2.15.** Possible configurations of the repeat unit with respect to the substrate for repeat units without (a) and with (b) $C_2$ symmetry.

configurations when polymer chains arrange on the substrate. However, in the case of a repeat unit possessing a $C_2$-axis perpendicular to the conjugation plane (Figure 2.15 b), the two possible configurations are equivalent. This will clearly aid in the packing of the main chains and reduce the stacking defects. More importantly, we have shown that good packing of the polymer chains is related to high mobility, and therefore can conclude that such $C_2$ symmetry of the repeat unit is necessary for high mobility. Such observation for a single family of conjugated polymers does not seem to constitute a design rule, but we carried out an extensive literature search and found overwhelming support for the $C_2$ symmetry design rule. Some of literature results are summarized in Table 2.3.

**Table 2.3.** High-performance polymer semiconductors and their reported mobility and repeat unit symmetry. Polymers with $C_2$ symmetry exhibit systematically higher field-effect mobility, as compared to similar polymers without the symmetry.

| Material | Field-effect mobility ($cm^2/Vs$) | $C_2$ symmetry | Reference |
|---|---|---|---|
| 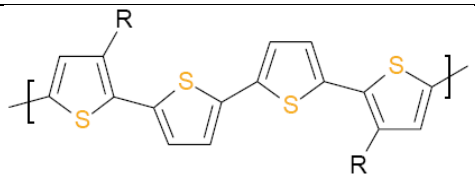 PQT-C12 | 0.06 – 0.12 (holes) | Yes | [15] |
| 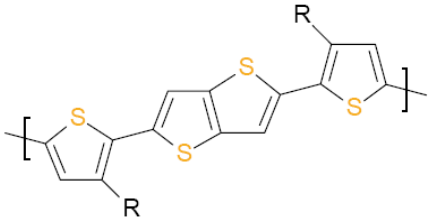 PBTTT | 0.2 – 0.6 (holes) | Yes | [16] |
| 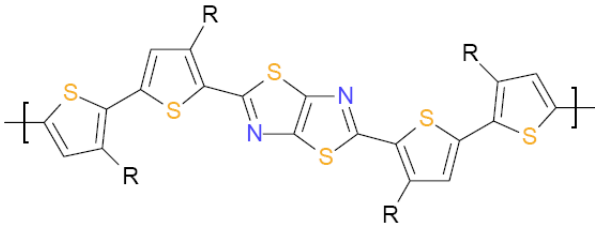 PTzQT | 0.01 – 0.3 (holes) | Yes | [39] |
| 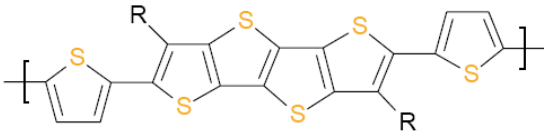 P2TDC13FT4 | 0.18 – 0.33 (holes) | Yes | [19] |
| 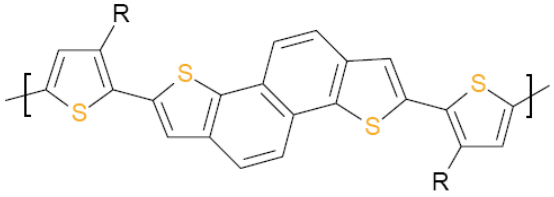 PNDTBT | 0.2 – 0.5 (holes) | Yes | [40] |

| | | | |
|---|---|---|---|
| 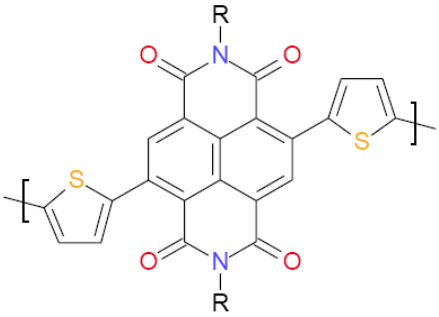 P(NDI2OD-T2) | 0.1 – 0.85 (electrons) | Yes | [41] |
| 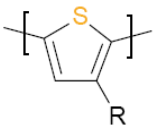 P3HT | 0.01 – 0.1 (holes) | No | [7] |
| 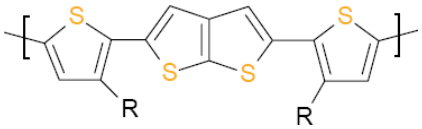 PBTCT | 0.03 (holes) | No | [42] |
| 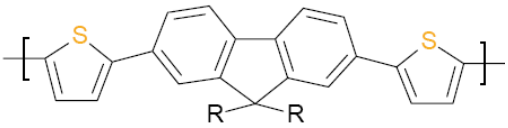 F8T2 | 0.001 – 0.01 (holes) | No | [43] |
| 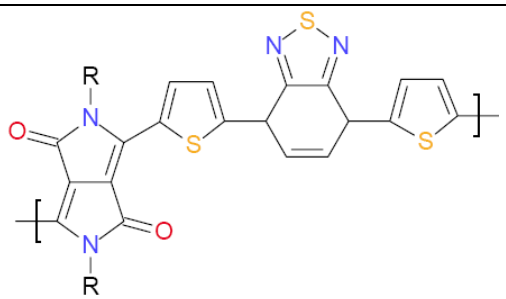 PDPP-TBT | 0.20 – 0.35 (holes)<br>0.16 – 0.4 (electrons) | No | [44] |

### *3. Thermal Stability of Materials*

With a good understanding of the effects of polymer structure on transport properties, we set out to investigate the effects of processing on polymer properties and stability.

Typically, polymeric materials are spin coated onto substrates from a solution of high boiling point solvents, in order to enhance crystallinity and electronic properties [45, 46]. The use of such solvents raises a concern regarding residual solvent in the thin film and its effect on thin film properties. Additionally, many conjugated polymeric materials tend to undergo a liquid crystal transition or side-chain melting between 100 °C and 200 °C, which encompasses the typical processing window for flexible substrates. Residual solvent and phase transitions make post-deposition annealing an important step in optimizing the structure and electronic performance of polymeric semiconductors, as such thin films tend to undergo both reversible and irreversible structural reorganization [47, 48].

For electronic applications, reproducibility is an important factor. Materials need to be controlled to prevent any undesired reorganization throughout the fabrication process with thermal processing steps upwards of 100 °C and device operation temperature, which is typically around 60 °Cfor an integrated device. Recent work on poly(3,3"-di-n-alkylterselenophene)-C10 has shown that while some phase transitions could be used to achieve improved ordering and electronic transport, they could also lead to detrimental changes in electronic properties such as a decrease in the field-effect mobility by an order of magnitude [49]. Cycling through a first-

order phase transition often introduces additional grain boundaries which may compromise device performance and lifetime.

Such findings seem to suggest that for flexible electronics, materials with phase transitions should be avoided due to potentially undesirable changes in the material's properties upon processing or otherwise serious limitations to the manufacturing processes. In the following section, we investigate the post deposition thermal annealing process *in-situ* and real-time, to identify possible processes contributing to film reorganization.

### *3.1 Experimental*

Two polymers, namely, poly(2,5-bis(thiophene-2-yl)-(3,7-ditri-decanyltetrathienoacene) (P2TDC13FT4) and poly(2,5-bis(thiophene-2-yl)-(3,7-dihepta-decanyltetrathienoacene) (P2TDC17FT4) were synthesized using previously published procedures [22, 19]. The structure of polymer is shown in inset of Figure 2.16. Molecular weights of polymers are summarized in Table 2.4.

**Table 2.4.** Molecular weight and polydispersity of P2TDC13FT3 and P2TDC17FT4.

| | $M_n$ | $M_w$ | polydispersity |
|---|---|---|---|
| P2TDC13FT4 | 9287 | 10680 | 1.15 |
| P2TDC17FT4 | 19596 | 21463 | 1.10 |

Standard differential scanning calorimetry (DSC) was carried out on the polymers using a TA Instruments Q1000 instrument with heating and cooling rates of 10 °C/min in order to identify possible transitions. Solutions of polymers in

dichlorobenzene at concentrations of 3 mg/mL were prepared by heating to 170°C for 30min with stirring to speed up dissolution. Silicon oxide substrates were cleaned by sonication in semiconductor grade acetone and isopropanol for 10 min in each solvent, and then given a 15 min air plasma treatment. Polymer thin films were then deposited by spin-casting at 1000 rpm for 60 s.

The microstructure of the polymer thin films was studied using Grazing Incidence Wide Angle X-Ray Scattering (GIWAXS) at D1 station of the Cornell High Energy Synchrotron Source (CHESS) facility. For GIWAXS measurements, the spin-coated films were annealed at various temperatures for 5 minutes. These films were then studied at the synchrotron, where scattering intensities were collected using a 2-D area detector (MedOptics). The samples were studied under various incident angles ranging from above the critical angle of the thin film to the critical angle of the silicon oxide substrate. Scattering vectors were calculated [50] and refraction corrected [28, 23]. Further *in-situ* annealing experiments were carried out inside a custom-built heating chamber set up at the D1 station. High purity helium gas was flowed through the chamber to create an inert atmosphere during the experiment. The films were annealed from 22 °C to 135 °C at approximately 15 °C intervals. During the annealing process, the films were maintained at constant temperature to within 1 °C between consecutive heating and cooling ramps for 5 minutes to allow the films to equilibrate as we collected GIWAXS patterns.

### *3.2 Results and Discussion*

***UV-Vis.*** Polymers were dissolved in chloroform, spin cast on quartz glass, and annealed at 160°C for 10 minutes in nitrogen atmosphere for optical absorption studies. Results are shown in Figure 2.16. P2TDC13FT4 and P2TDC17FT4 show absorption maxima at 545 and 538nm, with a shoulder peak at 584 and 576nm, respectively. A consistent red shift of the spectra for the polymer with shorter side-chains suggests a slightly better conjugation than the polymer with longer side-chains, with longer side-chains increasing the steric hindrance and disrupting the conjugation. The presence of a distinct absorption shoulder indicates long range order for both polymers.

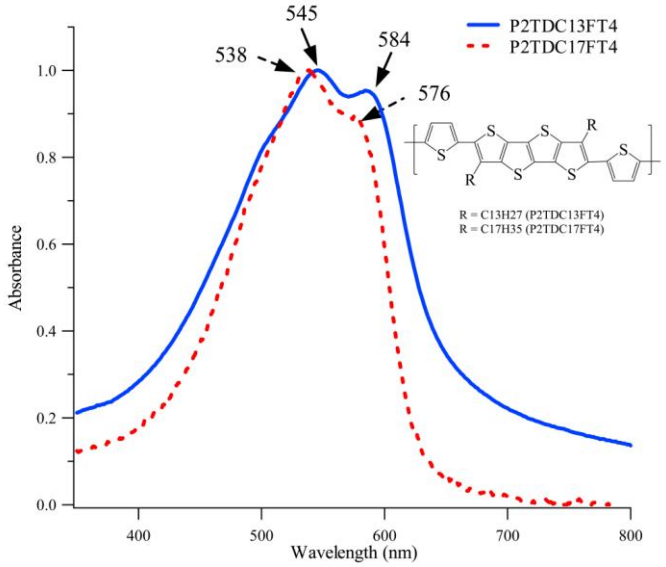


**Figure 2.16.** UV-Vis spectra of P2TDC13FT4 and P2TDC17FT4 spun from chlorobenzene solution on quartz and annealed at 160°C. Both polymers exhibit good interchain interaction and P2TDC13FT4 demonstrates slightly better conjugation than P2TDC17FT4.

***Thermal analysis.*** In the previous work on this fused thiophene ring polymer family, we investigated the role of the backbone on crystal packing and electronic performance, and in this section we extend our investigation of the correlation between polymer structure and thin film properties to the role of side-chain length and subsequent thermal annealing. We carried out differential scanning calorimetry on P2TDC13FT4 and P2TDC17FT4 in order to identify possible thermal transitions, which are quiet common in thiophene polymers. Surprising, we observed no obvious exothermic or endothermic transitions from DSC of the tetrathienoacenes above room temperature (Figure 2.17). We observed that P2TDC17FT4 has only one clear transition around 15 °C, while P2TDC13FT4 has no clear transitions. In addition, both polymers may have transitions upon heating and cooling around 110 °C and 200 °C, which suggests the possibility of thin film reorganization that could improve the crystallinity and/or electronic properties and warrants a detailed study. Unfortunately the transition temperature of 15 °C in P2TDC17FT4 was not accessible for our current analysis. It should be noted that the polydispersity of the synthesized polymers is around 1.1 for P2TDC17FT4, and 1.15 for P2TDC13FT4, and thus would not lead to suppression of distinct transition peaks in the DSC data. The possible transition temperatures and break-down temperatures serve as our guidelines in optimizing thin film processing through thermal annealing.

The endothermic peak around 15 °C from P2TDC17FT4 DSC data may be attributed to the side-chain melting. The absence of such peak for P2TDC13FT4 could be attributed to the inability of the shorter alkyl side-chains to crystallize.

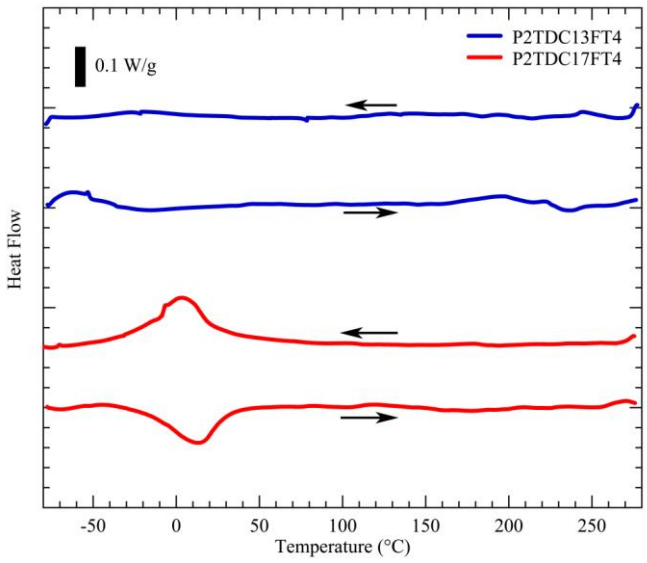


**Figure 2.17.** Second heating and cooling cycle DSC data for P2TDC13FT4 and P2TDC17FT4 polymers. P2TDC17FT4 exhibits a clear transition at 15°C, while the bump upon heating in P2TDC13FT4 at -60°C is due to the heating swing.

Chabinyc pointed out the similarity of conjugated polymers with rigid rod polymers with flexible side-chains [51]. Shi et al. presented a detailed analysis of a rigid rod polymer with flexible alkyl side-chains, that showed a similar alkyl-ordering temperature for 18 methylene groups; their transition temperature for side-chains with 14 methylene lies below -30 °C [52]. Hence it is also possible that alkyl chain ordering will occur in P2TDC13FT4 significantly below room temperature which was not accessible in our DSC instrument.

It has been previously found that in rigid rod polymers with alkyl side-chains the non-crystalline part of a side-chain is around 9-13 methylene groups [53, 54, 55]. The low value of the alkyl chain melting temperature in P2TDC17FT4 is an indication that the crystalline part of the alkyl chains must be very short. In the case of our

polymers, the large backbone repeat period (18.4 Å) due to the fused-ring thiophene moieties results in a large spacing between the alkyl side-chain anchor points and could act to increase the non-crystalline length of the side-chains to such extent that side-chains made up of 13 methylene group do not form significant crystalline region. Thus, P2TDC13FT4 would not exhibit a crystalline transition, as compared to P2TDC17FT4 with significantly longer side-chains.

***GIWAXS.*** In order to determine the effects of thermal annealing on polymer thin films, we utilized a combination of ex-situ and in-situ GIWAXS measurements and analyzed and quantified the structure of the thin films. For GIWAXS measurements, samples were spin cast on pre-cleaned silicon wafers as previously described. Subsequently, ex-situ samples were annealed at 150 °C, 240 °C, or 350 °C for 5 minutes inside a nitrogen glove box. P2TDC13FT4 polymer thin films were only annealed up to 240 °C, because further annealing caused polymer degradation. Similarly P2TDC17FT4 films were not annealed past 350 °C to prevent polymer break down. From the acquired 2-D GIWAXS patterns, the scattering intensities along $q_z$ and $q_{||}$ directions were extracted for P2TDC13FT4 and P2TDC17FT4 (Figure 2.18). Extracted patterns comply with the existing models for lamellar packing of conjugated polymer chains with the backbone aligned parallel to the substrate and the side-chain arrangement dominating the lamellar spacing perpendicular to the substrate.

For the temperature series of P2TDC13FT4, we observed that the diffraction peaks along the $q_z$ direction—and therefore the lamellar spacing—shift from 16.7 Å to 17.9 Å upon annealing at 150 °C, and then remained practically constant upon further

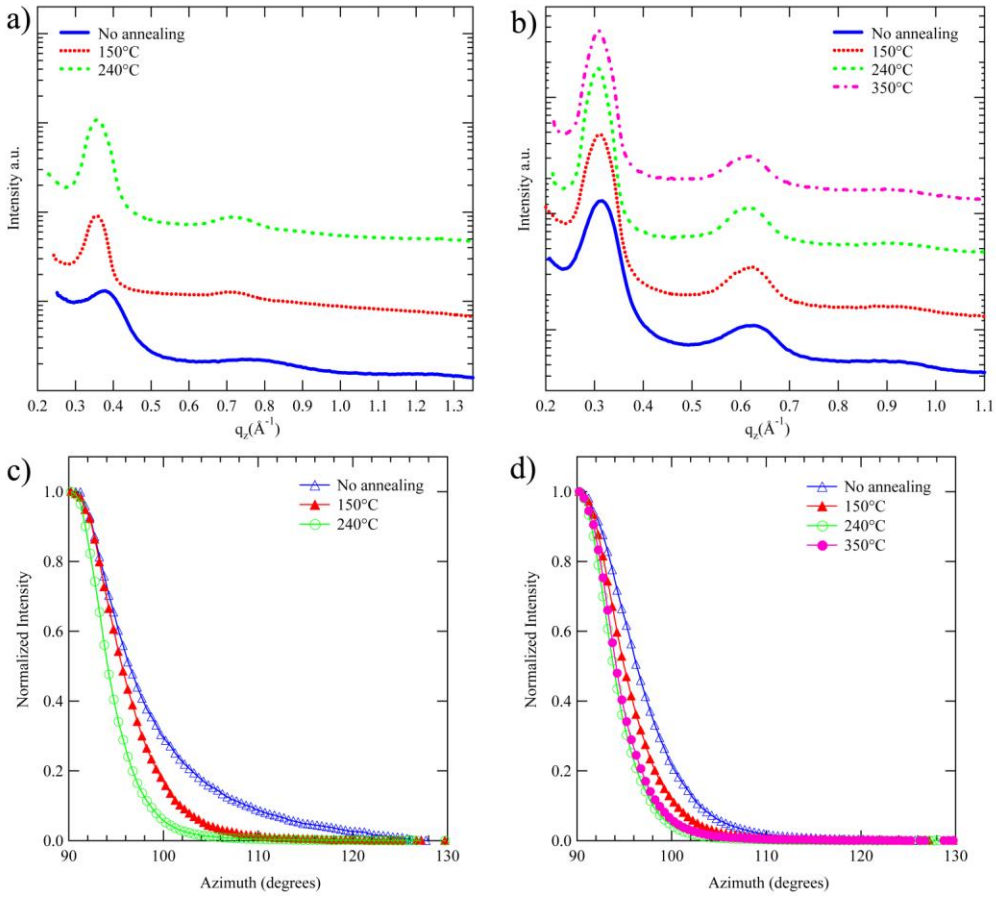


**Figure 2.18.** Extracted intensity along the $q_z$ direction of the P2TDC13FT4 (a) and P2TDC17FT4 (b) polymer films cast on $SiO_2$ surface with post-deposition annealing. The lamellar spacing in P2TDC13FT4 polymer increases upon annealing at 150 °C, while P2TDC17FT4 does not show any lamellar spacing changes upon annealing. Azimuth distribution of the (001) peak of P2TDC13FT4 (c) and P2TDC17FT4 (d) films annealed at various temperatures. Both polymers show improved lamellar alignment from the reduced mosaicity upon thermal annealing.

annealing. Performing the microstructure analysis and using the Scherrer formula with geometric correction [24], we calculate the correlated thickness of the lamellar stack to be 4.8, 11.1, and 7.8 lamellae for a film with no annealing, annealing at 150 °C, and 240 °C, respectively. In addition, we were able to examine the mosaicity of the films by plotting the azimuth distribution of the (001) peak. The full width at half maximum (FWHM) of the azimuth distribution was 12.8°, 11.2°, 8.2° for P2TDC13FT4 films with no annealing, annealing at 150 °C, and 240 °C, respectively. Such a small FWHM indicates well ordered parallel lamellae with small mosaicity. Based on the microstructure analysis of P2TDC13FT4, the optimum post-deposition annealing temperature which maximizes the lamellar correlated thickness, minimizes the mosaicity, and achieves a stable lamellar spacing appears to be between 150 °C and 240 °C.

Similar analysis of P2TDC17FT4 films revealed no change in the lamellar spacing upon thermal annealing, which remained constant at 20.4 Å. Lamellar stack heights of 5.7, 7.6, 13.0, and 9.6 lamellae were found for films with no annealing, annealing at 150 °C, 240 °C, and 350 °C, respectively. Additionally, the FWHM of 12.6°, 10.0°, 7.7°, and 8.3° were calculated for P2TDC17FT4 films with no annealing, annealing at 150 °C, 240 °C, and 350 °C, respectively. Similarly to P2TDC13FT4, P2TDC17FT4 forms well ordered parallel lamellae and we can conclude that the annealing temperature for the optimal thin film crystallinity of P2TDC17FT4 must be near 240 °C.

In order to better understand the dynamics of thermal reorganization observed in the case of P2TDC13FT4, we carried out in-situ thermal annealing experiments of

P2TDC13FT4 thin films at D1 station at CHESS, which allowed us to monitor the changes in the lamellar spacing as a function of annealing temperature. Extracted lamellar spacings during the in-situ annealing are plotted in Figure 2.19 as a function of temperature. From the heating curve, we observed that the polymer swells upon thermal annealing similarly to solvent annealing [56]. Around 60 °C, we observe a change in the thermal expansion trend of the lamellae. A similar behavior was observed during the cooling cycle at nearly the same temperature, but in that case we observed no changes in the lamellar spacing upon further cooling below 60 °C. Observed lamellar spacing changes are consistent with our previous ex-situ results and represent a 7% expansion from the original spacing. Calculating the linear thermal expansion coefficient from the linear part of the heating and cooling curves, we obtained $2\times10^{-4}$ Å/Å°C, which is at least an order of magnitude higher than expected for a polymer system. In addition to lamellar spacing expansion during thermal annealing, we also observe a reversible contraction in the π-π stacking distance up to 70 °C (see Figure 2.19), at which point the π-π stacking peak becomes too weak to be observed due to the Debye-Waller effect.

The difference in the optimal annealing temperature for the two polymers can be explained by the difference in side-chain length, with longer side-chain polymers requiring higher temperatures to reorganize. At the same time, it is important to point out that a change in d-spacing and thus lamellar reorganization upon annealing only occurs in the case of P2TDC13FT4 polymer films and not P2TDC17FT4, which suggests that the shorter side-chains are responsible for thin film reorganization upon annealing. Such structural reorganization, with expansion upon annealing, has been

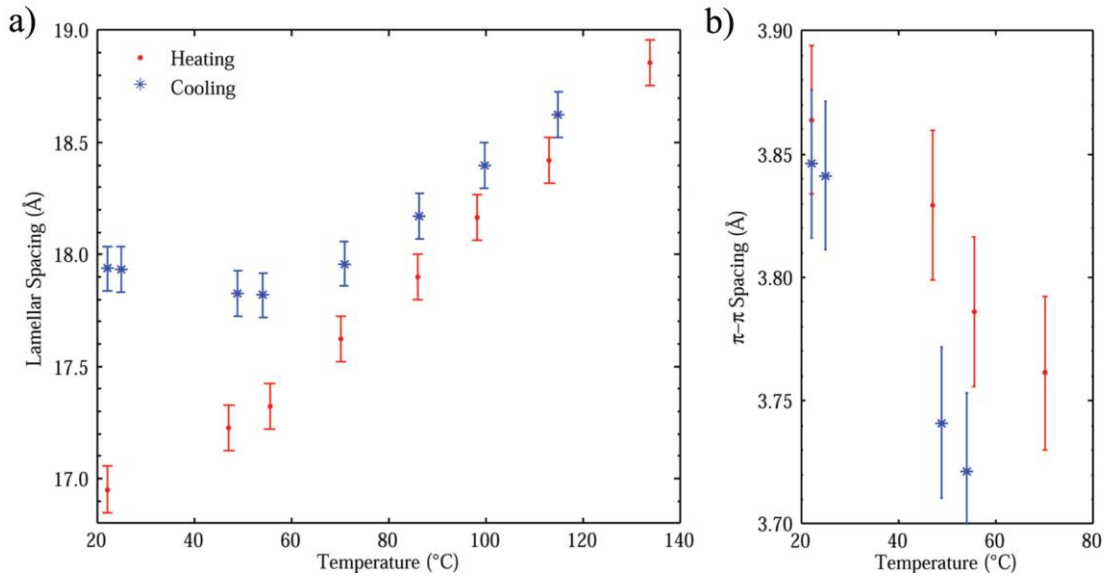


**Figure 2.19.** (a) A plot of lamellar spacing as a function temperature of P2TDC13FT4 upon heating and cooling. (b) A plot of the π-π stacking distance as a function of temperature of P2TDC13FT4 upon heating and cooling.

previously observed in other thin films of polythiophenes, like PBTTT [27], PQT-12 [15, 57], and PTzQT-12 [58]. However, contrary to our polymer, all of the previously mentioned polythiophenes undergo a liquid-crystalline phase transition, which leads to the expansion in the lamellar spacing. A detailed study of PBTTT shows that the expansion in the lamellar spacing is not gradual, but rather abrupt near the transition temperature [51].

Neither one of the characteristics of the typical polythiophene transitions matches the properties of our observed structural reorganization. Frequently, changes in the lamellar spacing are attributed to residual solvent evaporation upon sample annealing, but this would lead to a contraction with regard to expected lamellar spacing, as the solvent incorporated into the film is removed. This is contrary to the effect observed in our films and requires an alternative explanation. In order to further

rule out the possibility of solvent effects, we utilized vacuum annealing. High vacuum ($10^{-6}$ Torr) causes boiling point depreciation, with the boiling point of common solvents dropping to below room temperature. This enables us to drive out the excess solvent without adding any energy to the system, which could otherwise drive conformational changes.

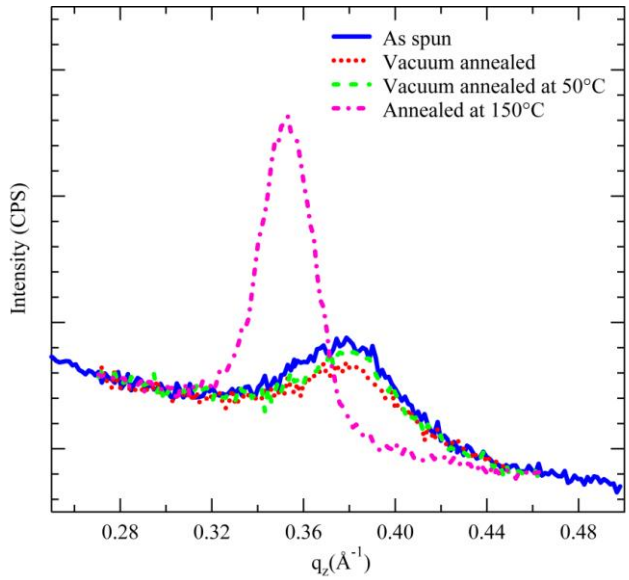


**Figure 2.20.** XRD patterns of the P2TDC13FT4 polymer film on $SiO_2$ surface as spun, after 13 hours of vacuum annealing, after 13 hours of vacuum annealing at 50 °C, and after 10 minutes annealing at 150 °C in nitrogen atmosphere.

The effects of vacuum annealing on polymer thin film structure were analyzed using X-ray diffraction, as shown in Figure 2.20. Spun cast samples with no vacuum or thermal annealing had lamellar spacing of 16.5 Å. After vacuum annealing for 13 hours, no change in the lamellar spacing was observed. Further vacuum annealing with samples heated to 50 °C for another 13 hours to ensure that no solvent remained,

caused no changes in the lamellar spacing. However, once the sample was annealed in nitrogen filled glove box at 150 °C for 10 minutes, the lamellar spacing increased to 17.9 Å. The lack of lamellar spacing changes during vacuum annealing, even at slightly elevated temperatures, rules out the possibility of residual solvent causing the lamellar reorganization upon thermal annealing for P2TDC13FT4. In addition, we observed a significant reduction in the peak width at half maximum upon thermal annealing, indicating improved ordering.

Our literature search produced a number of similar systems that undergo thermal expansion with better-understood dynamics, which help shed light on the transformation in polythiophenes. In block copolymer films, expansion of the unit cell in the Z direction has been noted before. For those systems, the high boiling point solvent has been attributed as the cause for a unit cell contraction due to slow solvent evaporation [59]. Roll-casting of triblock copolymer films has been shown to result in a stressed conformation, the annealing of which causes reorganization to a less stressed conformation [60]. Using in-situ Small Angle X-Ray Scattering (SAXS), thermal annealing of block copolymer films has shown a reorganization of such stressed film to a relaxed conformation upon heating to 80 °C.

In our case of P2TDC13FT4 we observe both reversible and irreversible thermal expansion of the lamellar stack, which differs from the results of the SAXS thermal work on roll-processed triblock copolymers, where an approximate 9% expansion of the lamellar spacing was observed without any observable thermal expansion upon further annealing. In addition, work on rigid rod polymer with flexible side-chains, 2,5-bis(hexadecyloxy)-1,4-phenylene diisocyanate (PI-16), has

shown a similar anomalous monatomic layer spacing increase with temperature up to a mesophase around 200 °C [61]. This suggests that the irreversible expansion of the lamellar spacing in P2TDC13FT4 can be attributed to relaxation due to contraction upon spinning from high boiling point solvent, but some process beyond relaxation upon thermal annealing is taking place in our system to achieve the reversible thermal behavior.

In a simple geometric lamellar stacking model inspired by Kline et al [38], the lamellar period was determined by the backbone contribution, side-chains orientations, and uninterdigitated region (see Figure 2.21). Using data on the lamellar spacing of the annealed tetrathienoacenes with various length side-chains, we can extrapolate the side-chain contribution to the lamellar spacing and therefore, determine a range of possible side-chain tilt angles. The alkyl side-chains of the P2TDC13FT4 account for approximately 10.9 Å of the lamellar spacing of the annealed thin films, suggesting a tilt angle of 48° with nearly fully interdigitated side-chains. This results in lamellar packing with a significant tilt of the side-chains. Based on this result, we hypothesize that during thermal annealing, the polymer chains reorganize by aligning the side-chains more vertically to the substrate. This conformation change would explain the significant change in the lamellar spacing, but also suggests that as side-chain tilt decreases, the hindrance between in-plane stacked polymer units would decrease and promote tighter π-π stacking of polymer units. In fact, we do observe a contraction in the π-π stacking distance (See Figure 2.19 (b)). This correlation between the π-π stacking and lamellar spacing, as well as the extreme side-chain tilt

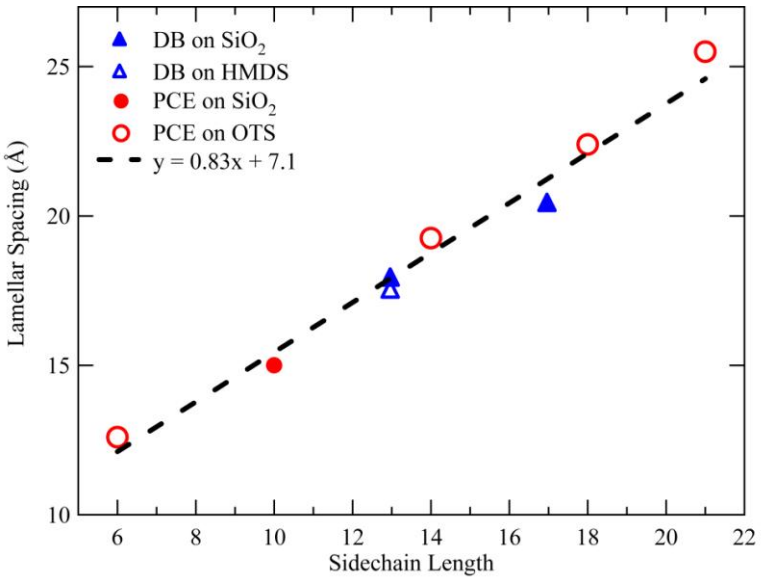


**Figure 2.21.** Lamellar spacing for various side-chain length variations of P2TDC*xx*FT4 polymer films after 150 °C thermal annealing. The solid triangles represent polymer thin films deposited from 1,2-dichlorobenzene (DB) on $SiO_2$ and open triangle represents film deposited on hexamethyldisilazane (HMDS) treated $SiO_2$. The solid circles represent polymer thin films deposited from pentachloroethane (PCE) on $SiO_2$ and open circles represent films deposited on octyltrichlorosilane (OTS) treated $SiO_2$. Linear extrapolation shows backbone and uninterdigitated space contribution of 7.1 Å. Solvent and substrate treatment appear to have little influence on the lamellar spacing.

angle, seems to support our hypothesis that alkyl side-chain conformation change leads to changes in the lamellar spacing upon thermal annealing.

These simple geometric arguments need to be used with caution, as DSC showed that the alkyl side-chains are for the most part disordered. Hence at best short-range order can be expected in the side-chain layer. However, infrared spectroscopy [62, 63] as well as molecular dynamics studies [64] have revealed in similar polymers that the density of gauche defects along the alkyl chains is small, i.e. the alkyl chains are mostly in a linear conformation, albeit translationally disordered. Hence the geometric model is still of use in providing an estimate of the average chain tilt.

It is important to point out that we do not observe any lamellar reorganization in P2TDC17FT4, which we attribute to increased lamellar stability facilitated by longer side-chains. Longer side-chains increase the interaction between lamellar stacks and inhibit unit cell contraction upon spin casting, as observed for shorter length side-chains. The observed thermal annealing effect in P2TDC13FT4 does not correlate to the expected transition temperatures predicted from DSC data.

### *3.3 Conclusion*

We observe an irreversible 7% expansion in the lamellar spacing for short side-chain length polythiophene system upon thermal annealing with a linear thermal expansion coefficient in the direction normal to the substrate on the order of $2\times10^{-4}$ Å/Å°C. After the initial relaxation from the contracted state due to casting conditions, P2TDC13FT4 displays a reversible linear thermal behavior of up to a measured temperature of 140 °C. Based on in-situ measurements and modelling, we attribute the

irreversible lamellar reorganization to unit cell contraction upon spin casting from high boiling point solvent, and the high thermal expansion coefficient to conformation changes in side-chain packing. Lack of distinct features in the DSC data suggested no changes in the thin film above room temperature, but that does not prove to be true in the case of our system. Further experiments showed that the removal of residual solvent upon thermal annealing does not play a role in polymer film reorganization in our system. This demonstrates the importance of X-Ray characterization of thin films to identify lamellar reorganization, which otherwise could lead to unexplained thin film property variations.

Observed thermal behavior of P2TDC13FT4 and P2TDC17FT4 shows stability of the polymer films over a large temperature range with no abrupt changes in film properties, making it an excellent candidate for organic electronics. Absence of phase transitions above room temperature, insures thin film stability upon processing, which could withstand photoresist baking or thermal curing of passivation layers [65, 66, 67] at a typical temperature of 100 °C. This distinguishes our polymers from P3HT, PBTTT, PQT, PTzQT, and others which have transitions in the standard processing window and require careful attention to ensure minimal changes to thin film morphology, as not to cause any undesired changes in device performance.

***4. Outlook***

In this section we have investigated the role of different components of polymeric semiconductors on thin film properties and transport. Additionally, we proposed a design criterion for polymer structure in order to achieve optimal thin film

packing and electronic transport. Further, the investigation of the thermal stability of our polymer revealed processing steps needed to produce a stable film. Based on the results of all this work, we fabricated thin film transistors of P2TDC13FT4 and P2TDC17FT4 on OTS treated $SiO_2$, which have shown little degradation over a 12 month period. Transfer curves in Figure 2.22 demonstrate the lack of change in the transfer curves of the devices over the year, as the samples were stored with environment with 30% relative humidity.

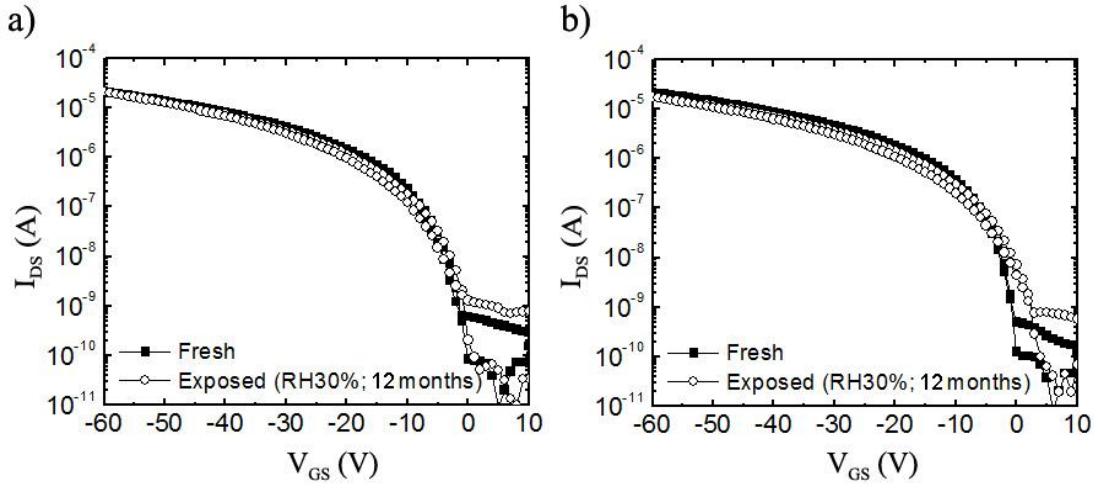


**Figure 2.22.** Transfer curves of transistors of P2TDC13FT4 (a) and P2TDC17FT4 (b) on OTS as fabricated and after aging, showing no significant degradation.

CHAPTER 3

MOLECULAR SEMICONDUCTORS

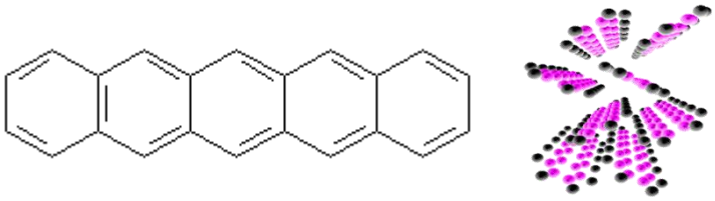

**Figure 3.1.** Pentacene ($C_{22}H_{14}$) structure (left) and herring-bone unit cell configuration (right).

### *1. In-Situ Growth*

Compared to polymeric semiconductors, molecular semiconductors have been studied for a much longer time and seem to be better understood. Among the highest performing molecular semiconductors is pentacene ($C_{22}H_{14}$), which is composed of five fused benzene rings, as shown in Figure 3.1. Much of the recent work on pentacene has been focused on growth by thermal evaporation on flexible substrates and various dielectrics. The best pentacene thin film transistors have been shown on $Al_2O_3$ dielectrics deposited by atomic layer deposition (ALD) with field-effect mobility of 1.5 $cm^2/Vs$ [68]. While ALD deposition does produce very smooth dielectric surfaces, the process is self-limiting and time consuming. A more practical dielectric, which would also be compatible with organic electronics, is spun-on polymer dielectric. As we have alluded to previously, reproducibility is very desirable in the manufacturing process and one of the most uniform and consistent spin-on materials is photoresist. Photoresists are extensively used by the semiconductor industry and are manufactured with the smallest allowable variations in their properties. Such consistency and wide spread use make these materials an ideal

dielectric for use in organic electronics. For this reason, we investigated the growth and electronic performance of pentacene on three dielectric surfaces: $SiO_2$, HSQ (e-beam resist), and Shipley (negative tone, i-line resist).

### *1.1 Experimental*

Substrates used for pentacene deposition were highly p-doped Si <1 0 0> wafers, which were subjected to RCA clean, immediately followed be $SiO_2$ growth. RCA clean is a two step cleaning process used to remove contaminants from silicon wafers prior to high temperature processing. The first step of RCA clean, SC-1, is a wet etch in ammonium hydroxide and hydrogen peroxide bath at 75 °C to remove organic surface contaminants. The second step of RCA clean, SC-2, is a wet etch in hydrochloric acid and ammonium hydroxide bath at 75 °C to remove metals, alkali ions, and metal hydroxides. Each wet etch step is followed by a rinse in deionized (DI) water. Approximately 300nm of $SiO_2$ was grown using wet thermal oxidation at 1000 °C at the Cornell Nanofabrication Facility. Shipley negative tone resist was spun on some of the substrates and soft baked. These substrates were then UV flood exposed, in order to achieve complete polymer crosslinking. HSQ was spun on some of the substrates and as it is an e-beam resist, no changes to these samples were expected over the time period of the experiment.

Pentacene thin films were deposited in a custom built top source deposition chamber mounted at D1 beamline at CHESS. The chamber has a Beryllium window through which we conducted GIWAXS during the pentacene growth on various substrates. Pentacene was deposited at a flux of 0.1 Å/s to the total thickness of 500 Å or 32.5 pentacene monolayers (ML), using "thin-film" phase $d_{001}$-spacing of 15.4 Å [69]. The schematic of the deposition chamber is shown in Figure 3.2 below. The

topography of deposited pentacene films was investigated *ex-situ* using AFM in tapping mode within one hour of the completion of the growth.

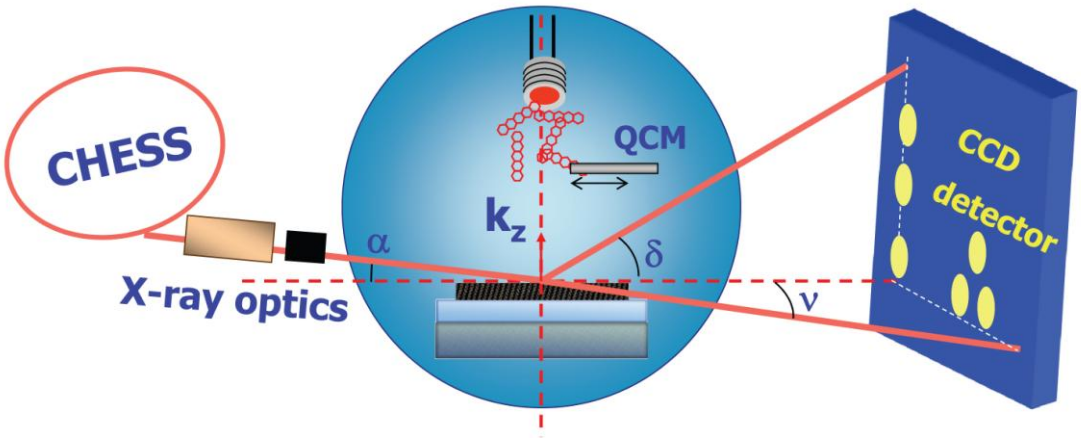


**Figure 3.2.** Custom pentacene deposition chamber with GIWAXS capabilities. Top deposition source allows for characterization of the thin film deposited on the substrate, which is aligned with the synchrotron X-ray beam for *in-situ* and real-time measurements of thin film growth.

Thin film field-effect transistors were fabricated by depositing Au top electrodes through a contact shadow mask to define devices with $W$ = 1 mm and $L$ = 75 μm. These devices were measured in a LakeShore vacuum probe station using LabView controlled Keithley SourceMeters. The analysis was carried out as previously described in Section II.1.1.

### *1.2 Results and Discussion*

Gathered GIWAXS data during pentacene growth shows the pentacene crystal structure during the deposition process. A few representative snapshot from the pentacene growth on $SiO_2$, HSQ, and Shipley dielectrics are shown in Figure 3.3.

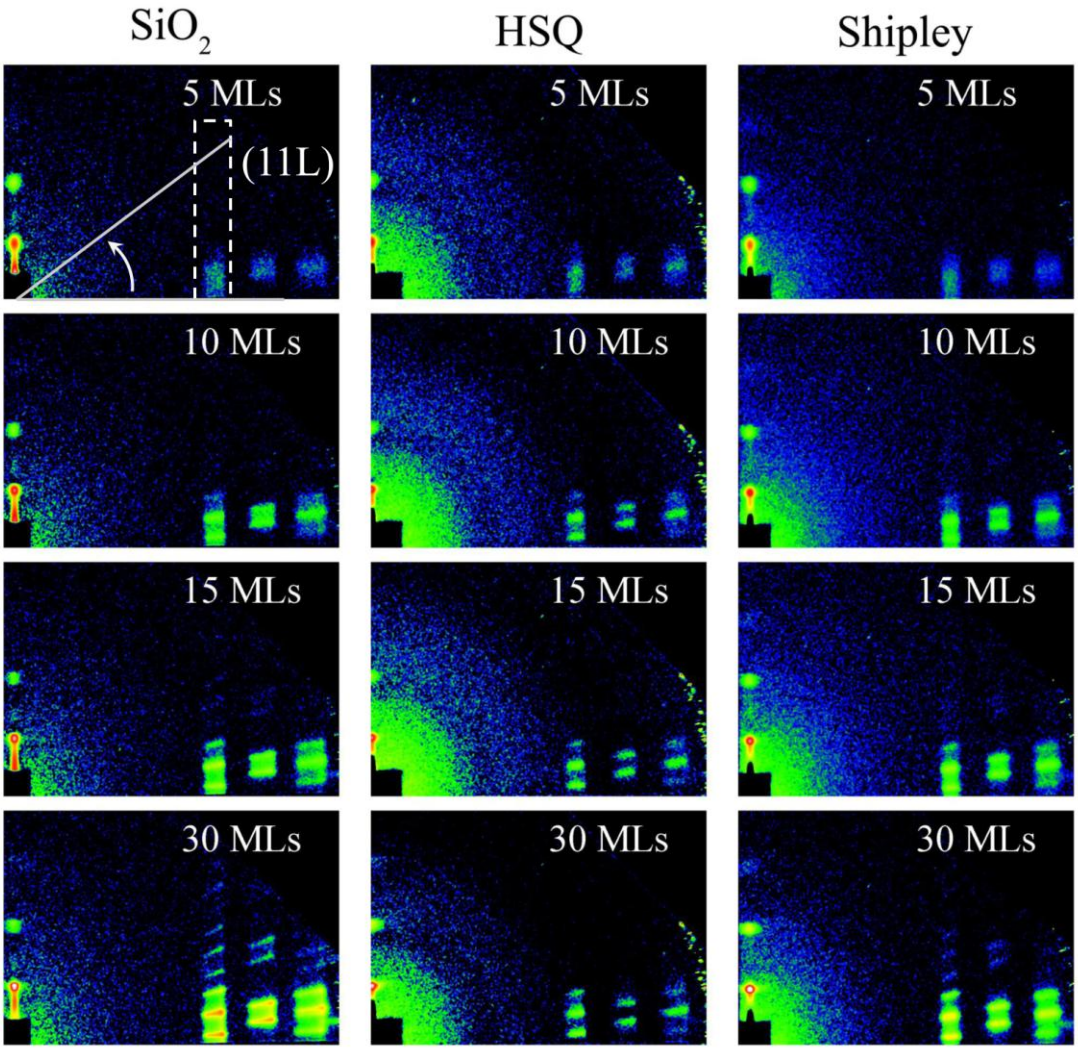


**Figure 3.3.** *In-situ* GIWAXS of pentacene growth on $SiO_2$, HSQ, and Shipley substrates. Pentacene thin films shows "thin-film" phase structure on all three substrates and no intermediate structures. (11L) crystal truncation rod was extracted for further analysis using radial integration as illustrated.

In order to get a better understanding of the progression of the pentacene crystal structure during the growth, we extracted the scattering intensity along the (11L) crystal rod as a function of deposition thickness for the three studied samples (Figure 3.4). (11L) was chosen, because it is most sensitive to unit cell changes, as evidenced from the structure of pentacene "thin-film" [70] and bulk phases [71], and has the highest scattering intensity. From 2-D GIWAXS and (11L) crystal rod, we observe no difference in the crystal structure formed on top of the three different surfaces. All three surfaces result in "thin-film" phase [70] growth of pentacene with no bulk phase [71] present. In addition, we do not observe any changes in the pentacene crystalline orientation, like in the case of *in-situ* growth of diindenoperylene [72, 73]. From the (11L) crystal rod, we are able to observe that the pentacene thin films on the three substrates differ in their crystallinity.

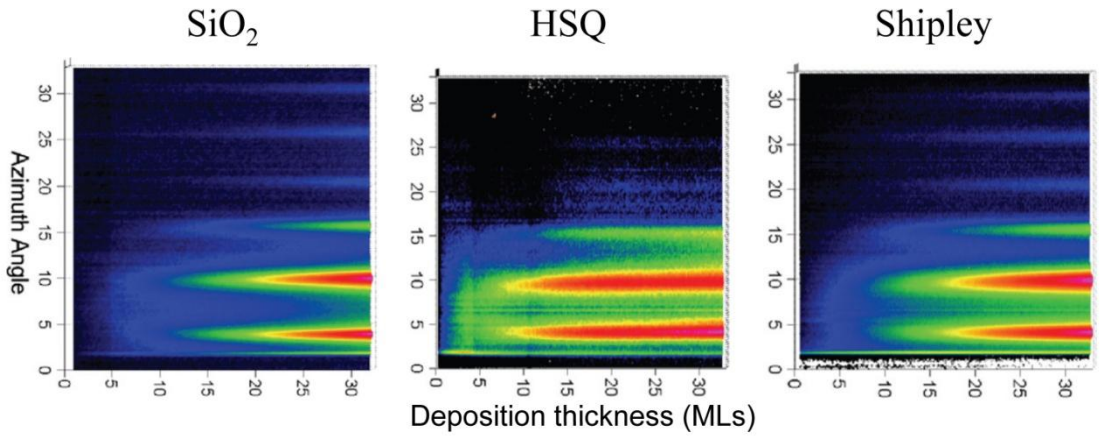


**Figure 3.4.** Development of pentacene (11L) rod as a function of deposition time for growth on $SiO_2$, HSQ, and Shipley substrates.

Additional details of the growth can be seen by extracting the correlated crystal thickness as a function of deposited material using Scherrer analysis on the (111) peak (Figure 3.5). Correlated crystal thickness refers to the average crystal thickness contributing to the coherent scattering and in our case best demonstrates the

differences between the crystallinity of the pentacene films on various surfaces. First of all, one might naively expect the crystal thickness to equal the amount of material deposited, which would follow the indicated linear trend. This is not the case in pentacene, one of the main reasons for which is that pentacene does not grow in a layer-by-layer fashion for more than a few monolayers (MLs) and the growth becomes more characteristic of Stranski-Krastanov type growth with formation of pyramidal crystallites. In case of pentacene grown on $SiO_2$, we observe that up to 15 MLs, pentacene crystal thickness follows a direct linear relationship with the amount of pentacene deposited. The crystal thickness growth slows after the deposition of the first 15 MLs, and at the final thickness of approximately 30 MLs, pentacene crystallite thickness is 20 MLs. In the case of pentacene grown on HSQ and Shipley, we observe a similar direct linear growth relationship for the first 10 MLs, after which the crystal thickness growth is dramatically reduced to nearly no further growth. At the final thickness of 30 MLs, the thickness of pentacene crystallites on HSQ and Shipley is 13 MLs and 15 MLs, respectively. The slowing in the correlated crystal thickness during the constant flux depositions suggests the possibility for secondary crystallite nucleation on top the existing crystallites or the impingement of crystallites, which inhibits their growth due to the strong anisotropy of pentacene growth [74]. The case of growth impingement would result from larger nucleation density on HSQ and Shipley, which can be verified by analyzing the thin film topography with AFM.

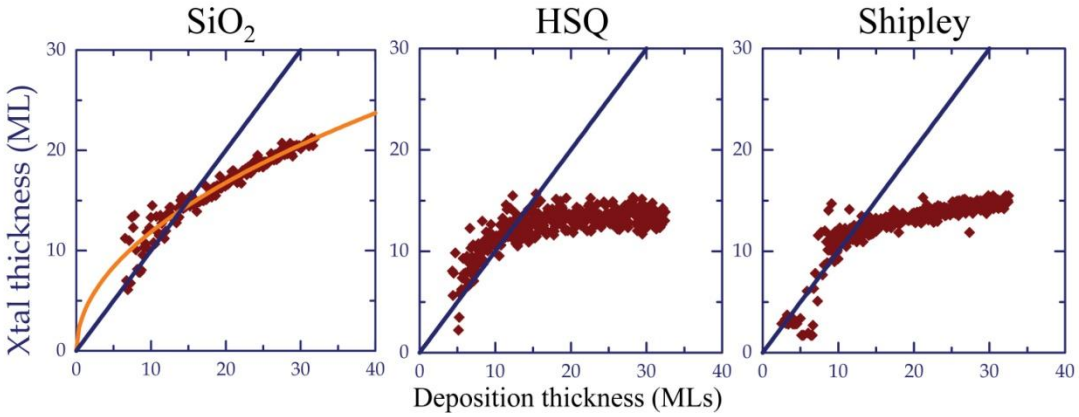


**Figure 3.5.** Correlated crystal thickness of pentacene film during film growth on $SiO_2$, HSQ, and Shipley substrates.

Measured topography of pentacene films on $SiO_2$, HSQ, and Shipley is shown in Figure 3.6. We observe a drastic difference between the topography on $SiO_2$ as compared to HSQ and Shipley. Pentacene on $SiO_2$ forms large grains, but on HSQ and Shipley the grain size is nearly 5-10 times smaller. Observed large grain size from AFM image is consistent with the observed large crystal thickness from GIWAXS data. Small grain size on Shipley and HSQ could be due to large initial nucleation density on those surfaces, as a result of increased interaction between the dielectric surface and pentacene or surface roughness.

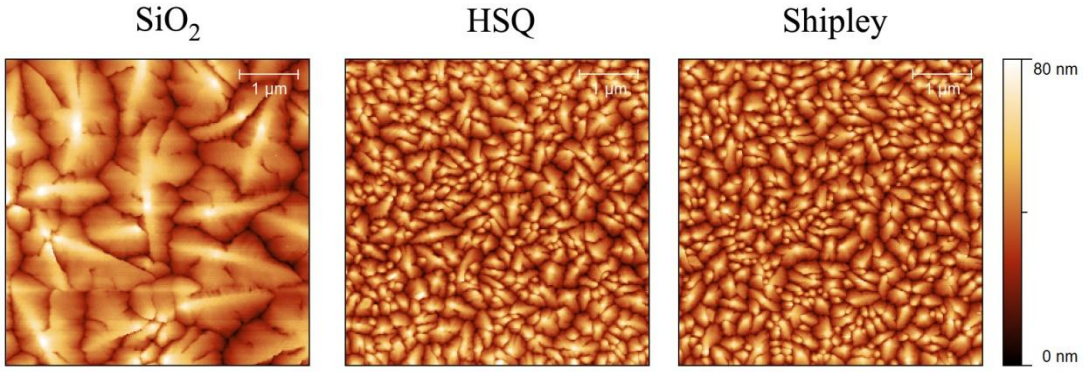


**Figure 3.6.** AFM of pentacene thin films (~32MLs) on $SiO_2$, HSQ, and Shipley.

Ultimately, we care to compare the thin film device performance of pentacene film on various dielectric surfaces and in Figure 3.7, we show the output curves of the fabricated field-effect transistors. The average calculated field-effect hole mobility from the linear saturation regime is 0.6 $cm^2/Vs$, 0.3 $cm^2/Vs$, and 0.01 $cm^2/Vs$ for pentacene on $SiO_2$, HSQ, and Shipley, respectively.

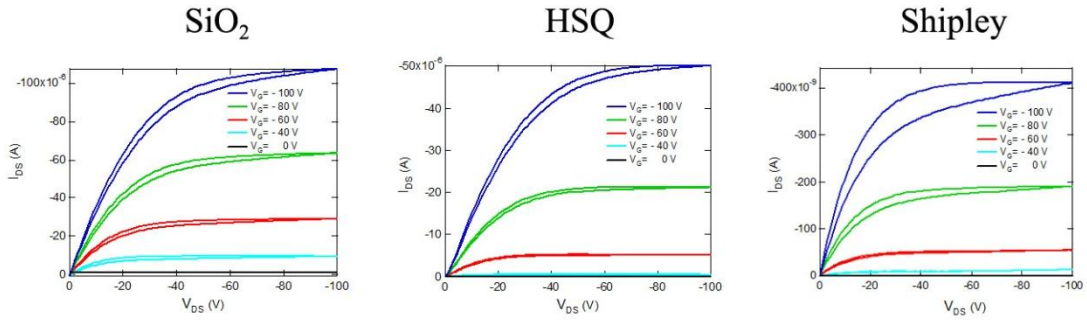


**Figure 3.7.** Output characteristic of pentacene top contact thin film transistors grown on $SiO_2$, HSQ, and Shipley.

It is quite surprising to note that the mobility on $SiO_2$ and HSQ are similar and differ only by a factor of 2, whereas their morphology and crystallinity are significantly different. On the other hand, the mobility on Shipley is more than an order of magnitude lower as compared to HSQ, but the morphology and crystallinity of pentacene film for those surfaces are quite similar. Such trend in field-effect mobility is difficult to explain.

Field-effect transport occurs at the interfacial organic layer, where the field induced by the gate potential is the highest. The number of MLs contributing to charge transport depends on the electrostatic field screening and, in some part, on morphology. In the case of pentacene, it has been demonstrated [75, 76, 77, 78] that only the first 4-5 MLs contribute to charge transport. This leads us to believe that the

properties of the pentacene films at the interface with $SiO_2$, HSQ, and Shipley are different and lead to corresponding differences in the observed field-effect mobility. Unfortunately, in this experiment we were not able to investigate the growth at early stages due to low signal to noise ratio.

### *1.3 Conclusion*

In this work, we explored the use of alternative dielectric surfaces, such as photoresist and e-beam resist, which are widely used in the electronics industry and allow for easy solution processing. Using *in-situ* and real-time GIWAXS measurements we monitored pentacene growth on HSQ e-beam resist and Shipley i-line photoresist. We observed no change in the pentacene crystal structure as compared to growth on the reference $SiO_2$ dielectric. Although, pentacene films on HSQ and Shipley did show decreased crystallinity and grain size. Surprisingly, the field-effect hole mobility was found to decrease only by a factor of 2 for pentacene on HSQ and by more than a factor of 15 on Shipley. Such relationship cannot be explained by the observed topography or crystallinity and suggests that the thin film properties of thick films (~30 MLs) are not indicative of the charge transport at the interfacial layer (4-5 MLs). Thus, a more careful study of the interface is required to understand charge transport on alternative dielectrics.

## *2. Growth on Modified Surfaces*

### *2.1 Introduction*

As seen from the last section on *in-situ* growth and numerous accounts in literature [75, 76, 77, 78], the carrier transport in pentacene thin films is severely affected by the dielectric-pentacene interface quality and the first few pentacene

monolayers. The Debye length in pentacene has been shown to be 4-5 MLs[79], and for this reason, the first few monolayers (ML) of pentacene are crucial to OTFT application. Recent work on pentacene has revealed that passivation of the dielectric interface with a coating, like hexamethyldisilazane (HMDS) or octadecyltrichlorosilane (ODTS) and others, produces systematically higher values of field-effect mobility for pentacene films deposited from thermal and supersonic molecular beam sources [80, 81].

The growth, structure, and morphology of thin films can be determined by combining one or more of *ex-situ* and/or *in-situ* methods, such as AFM, photoelectron, or low energy electron microscopies, and XRD. Most techniques mentioned above are surface sensitive, and therefore the value and validity of such studies are contingent upon the very thin organic films remaining static from the end of deposition through the characterization. Post-deposition reorganization of such film, by dewetting, intermixing, or Ostwald ripening can introduce significant errors and artifacts when characterization is performed some time after the deposition. In fact, there are examples of conflicting reporting on the growth modes of thin films of pentacene on various surfaces [82, 83]. In addition, the large range of surface energies created by the dielectric treatments, presents possibilities for thermodynamic film instabilities. For these reasons, we investigated the growth of ultra thin pentacene film on bare $SiO_2$, HMDS treated $SiO_2$, and FOTS treated $SiO_2$ by both *ex-situ* and *in-situ* methods.

### *2.2 Experimental*

Si <1 0 0> substrates were used for thin film growth and were cleaned as previously discussed. HMDS was deposited from the vapor phase using a YES LP-III vapor prime oven after successive dehydration cycles with substrate held at 150 °C.

FOTS was deposited from the vapor phase using the MVD-100 system with an additional $O_2$ plasma cleaning step prior to deposition.

Thin films of pentacene were thermally deposited in a high vacuum (~$6 \times 10^{-7}$ Torr) chamber inside a nitrogen filled glove box. The substrates were held at room temperature during deposition. The rate of deposition was 0.10 ± 0.01 Å/s as measured by a quartz crystal microbalance. Pentacene was also deposited from a supersonic molecular beam source for the *in-situ* study [84]. Ex-situ AFM was performed in air on samples less than 30 minutes after the removal of samples from the vacuum chamber, unless otherwise stated. The surface energy of HMDS and FOTS coated $SiO_2$ was calculated by measuring the contact angles of formamide and water, using the VCA Optima XE. Using these test liquids with known surface energies, $\gamma_L^d$ and $\gamma_L^p$, we determined the dispersive and polar components of surface energy of the substrate, $\gamma_S^d$ and $\gamma_S^p$, as well as the total surface energy, $\gamma_S = \gamma_S^d + \gamma_S^p$, by measuring the contact angle, $\theta$, and solving the simultaneous Owen, Wendt, Rabel, Kaelble equations (geometric mean) [85]:

$$\gamma_L(1 + \cos(\theta)) = 2\sqrt{(\gamma_L^d \gamma_S^d)} + 2\sqrt{(\gamma_L^p \gamma_S^p)} \qquad (2)$$

***In-situ time-resolved Anti-Bragg scattering.*** In Anti-Bragg configuration, the momentum transfer, $q$, is chosen such that $q \cdot d = \pi$, where $d$ is the interplanar spacing. This corresponds to the disallowed $(00^1/_2)$ reflection where the scattered intensity from the consecutive pentacene layers forms destructive interference. The destructive interference leads to increased sensitivity and has been used in the study of inorganic[86] and organic films[87, 72].

The scattering intensity for a thin film is then given by [88]:

$$I(t) = \left| r_{sub} e^{-i\varphi} + r_{film} \sum_n \theta_n(t) e^{-inq \cdot d} \right|^2 \qquad (3)$$

where $r_{sub}$ and $r_{film}$ are the scattering amplitudes of the substrate and the film, $\theta(t)$ is the coverage of the $n^{th}$ layer of film, and $\varphi$ is the phase difference between the substrate reflection and the thin film. The layer coverage of $n^{th}$ layer can be modeled using a version of the mean-field, rate equation growth model first proposed by Cohen *et al* [89].The equation for the layer coverage is given by:

$$\theta_n(t) = FS_{n-1}(\theta_{n-1} - \theta_n) - \alpha_{n-1}FS_{n-1}(\theta_{n-1} - \theta_n) + \alpha_n FS_n(\theta_n - \theta_{n+1}) \quad (4)$$

where $n = 0$ represents the substrate, $n = 1$ the first molecular layer, *etc.*, $S_n$ is the probability of adsorption for molecules incident on the $n^{th}$ layer, $F$ is the incident material flux, and $\alpha_n$ is the fraction of molecules that initially impact the $n^{th}$ layer, but become incorporated into that layer by some "downward" interlayer transport. Thereby in this model, the molecules that land on top of the *n-1* layer may diffuse and incorporate on the step edge of the $n^{th}$ layer, or transfer down to the top of the *n-2* layer to be incorporated into the *n-1* layer. Thermal desorption of molecules that have incorporated into a layer, as well as "upward" interlayer transport are neglected. These are valid assumptions for the materials we investigate, due to the high energy barrier to "upward" transport [87], and our processing conditions. Combining the time dependent layer coverages with equation (3) and fitting the Anti-Bragg scattering intensity, produces layer coverages as functions of time. These can be used to study the dynamics of thin films growth, as well as calculate the instantaneous surface roughness to be compared to *ex-situ* AFM results.

### *2.3 Results and Discussion*

***Ex-situ* study**. 1 – 2 MLs of pentacene were deposited on a cleaned $SiO_2$ surface by thermal deposition, kept at high vacuum for 5 and 120 minutes after

deposition, and then removed to air and imaged with AFM within 30 minutes. The topography of these two substrates (Figure 3.8) reveals a complete 1st ML with sparse islands of the 2nd ML. Besides the difference in deposited material, these two samples appear to be identical. Additionally, the sample kept in vacuum for 5 minutes was reimaged after 3 days in air and showed no significant change in surface morphology, which is quantified by surface roughness measurement ($\sigma_{AFM}$) in Figure 3.8 (c). These results, establish a control experiment with no post deposition film reorganization on $SiO_2$.

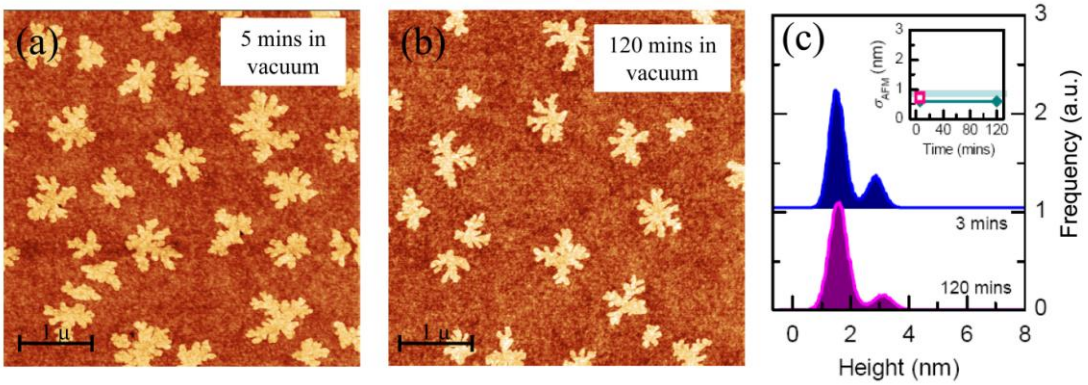


**Figure 3.8.** AFM micrographs of pentacene thin films on bare $SiO_2$.

Next, a similar set of experiments was carried out on HMDS treated $SiO_2$, where thin films were kept in high vacuum for 5, 40, 80, and 120 minutes following pentacene deposition. The pentacene thin film on HMDS kept in high vacuum for 5 minutes shows similarity to the results on $SiO_2$, with the exception of pit formation near the 2nd ML islands (see Figure 3.9). Thin films that were kept in vacuum longer show a progression of the film towards an islanded topography. The 1st ML becomes depleted, while islands 2, 3, and 4 MLs high islands begin to form. This appears to be reminiscent of partial dewetting. The evolution of this surface morphology change was quantified by calculating the surface roughness (Figure 3.9 (c) ). The plot

reveals a superlinear roughening behavior as surface roughness increases by a factor of 4 to 2 nm. This indicates an acceleration of the morphological changes with time spent in vacuum.

Additionally, the sample kept in high vacuum for 5 minutes and displaying the most similarity to the pristine films on $SiO_2$ was reimaged after 90 days in air and showed no significant changes (Figure 3.10 (a) ). This suggests that morphological reorganization does not occur in ambient air.

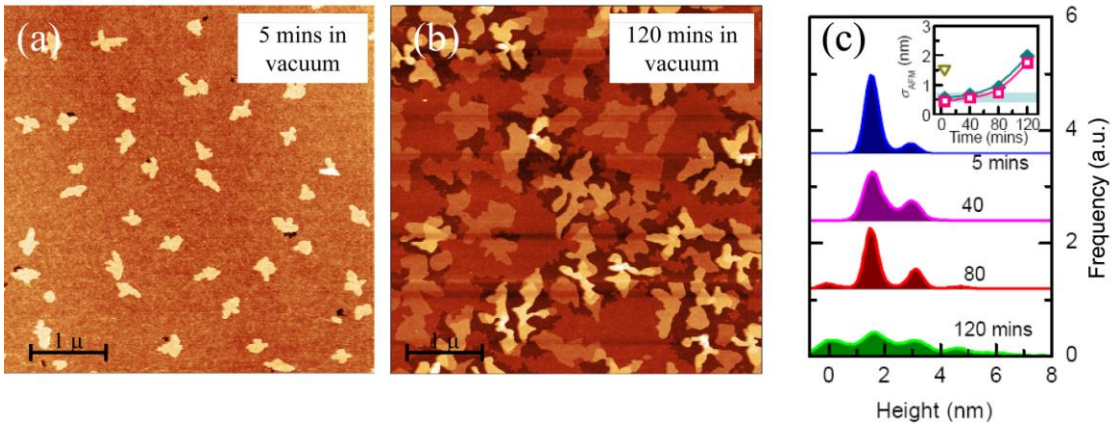


**Figure 3.9.** AFM micrographs of pentacene thin films on HMDS treated $SiO_2$.

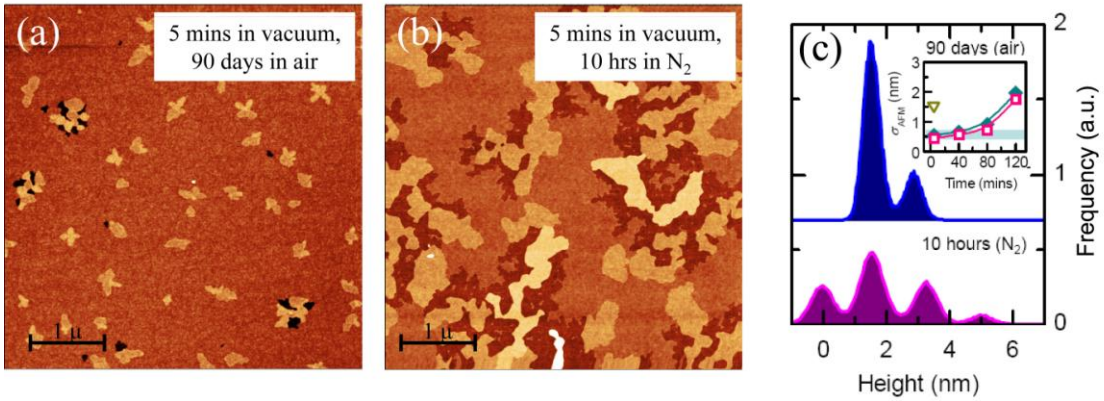


**Figure 3.10.** AFM micrographs of pentacene thin films on HMDS treated $SiO_2$ upon aging in air for 90 days (a) and nitrogen filled glove box for 10 hours (b).

In order to explore the potential role of $O_2$ and $H_2O$, a thin film of pentacene on HMDS treated $SiO_2$ was removed from vacuum 5 minutes after the deposition and stored in a nitrogen filled glove box for 10 hours, after which it was removed to ambient air and imaged within 30 minutes. Surface topography (Figure 3.10 (b) ) shows significant post-deposition reorganization, similar to the observed reorganization after 120 minutes in high vacuum. The difference between the post-deposition behavior of pentacene films on HMDS stored in the nitrogen glove box and ambient air suggests that oxygen and/or water vapor and/or light exposure may play an important role in stabilizing pentacene thin film morphology. A further test was conducted to examine the reversibility of pentacene reorganization, by depositing pentacene on HMDS treated $SiO_2$ and removing the sample into ambient air for AFM imaging after 5 minutes in high vacuum. After initial AFM imaging, the sample was placed back under high vacuum and re-imaged after 2 and 24 hours. No thin film reorganization was observed in this case, suggesting that exposure to ambient air causes permanent quenching of morphological reorganization of thin films of pentacene on HMDS treated $SiO_2$.

Further investigation of 1 ML thin films of pentacene was carried out on FOTS treated $SiO_2$. Thin films grown on FOTS and kept under high vacuum for 5 and 120 minutes after deposition are shown in Figure 3.11. AFM images reveal a significantly different morphology to the one observed on HMDS and bare $SiO_2$. The morphology is characterized by 2 – 6 ML high islands with as much as 40% of the substrate exposed. The aging of pentacene films on FOTS reveals a relatively small shift in surface roughness for an initially rough surface. Aging of the pentacene thin film in ambient air for 90 days reveals a small morphology change as well. This is in contrast to the results on HMDS treated substrate, where no changes were observed after similar aging in air.

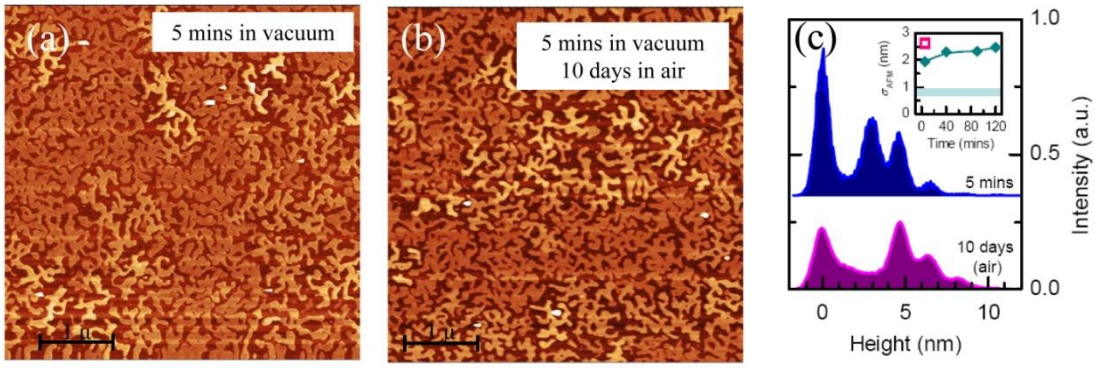


**Figure 3.11.** AFM micrographs of pentacene thin films on FOTS treated $SiO_2$.

Surface roughness of pentacene films on FOTS is four times larger than on HMDS. Such a striking difference between the two results suggests that either pentacene undergoes a Volmer-Weber type growth on FOTS or that the growth is layer-by-layer as on $SiO_2$, but the morphological reorganization occurs over a much faster time scale on FOTS. Based only on *ex-situ* characterization, we refrain from making any kind of unsupported conclusion about the growth on FOTS and in place, utilize *in-situ* Anti-Bragg Scattering to aid in understanding the differences between the two thin films.

***In-situ* study.** Growth dynamics of pentacene growth on $SiO_2$, HMDS treated $SiO_2$, and FOTS treated $SiO_2$ were studied using time-resolved X-ray Anti-Bragg Scattering at the G3 hutch at CHESS. Pentacene was deposited using a supersonic molecular beam source rather than a thermal source. At low energy depositions the supersonic beam is a sufficiently good comparison [90, 91] to thermal deposition to investigate the growth dynamics and dewetting observed by AFM.

Acquired Anti-Bragg oscillations were fitted with the previously discussed growth and scattering models and calculated layer coverages and predicted surface roughnesses ($\sigma_{XRR}$) as a function of total material deposited are shown in Figure 3.12.

The mean-field growth behavior appears to be almost identical on all surfaces for ultra thin films. We observe that in all cases the first monolayer grows to a coverage of nearly 80%, before the second monolayer nucleates, which is similar to the previous report of pentacene growth on $SiO_2$ [84]. In addition, clear oscillations and a decrease in roughness on all three surfaces around 1 ML film thickness indicate that all three films grow initially layer-by-layer. Beyond 2 ML film thickness, pentacene growth on FOTS tends to result in larger surface roughness ($\sigma_{XRR}$) and the dampened growth oscillations suggesting a greater tendency to undergo 3D growth than on bare $SiO_2$ or HMDS treated $SiO_2$. However these differences are modest and do not necessarily indicate a dramatic change in the growth behavior.

Observed surface roughness from *ex-situ* AFM measurement is significantly different from the predicted roughness from *in-situ* growth in the case of FOTS treated $SiO_2$ and HMDS treated $SiO_2$, where the samples have clearly been dewetting as observed by AFM, confirming that significant dewetting has occurred in both cases. This result is significant and would not be otherwise possible without the use of *in-situ* technique, demonstrating the important of *in-situ* experiments to supplement *ex-situ* measurements, in order to avoid erroneous conclusions due to overlooked thin film reorganization.

We extended this study by analyzing thicker films of pentacene on the three surfaces, and computed the difference in surface roughness attained from *ex-situ* AFM ($\sigma_{AFM}$) and the expected surface roughness from growth dynamics ($\sigma_{XRR}$), see Figure 3.13. Such difference is typically within 10% for pentacene films deposited on $SiO_2$ for various thicknesses. The difference is much larger and consistently positive on HMDS and FOTS treated $SiO_2$ going up to the measured 150% error. Figure 3.13 demonstrate that for thicker films the difference between the roughness measurements decreases and is within 10% after the deposition of 5 ML.

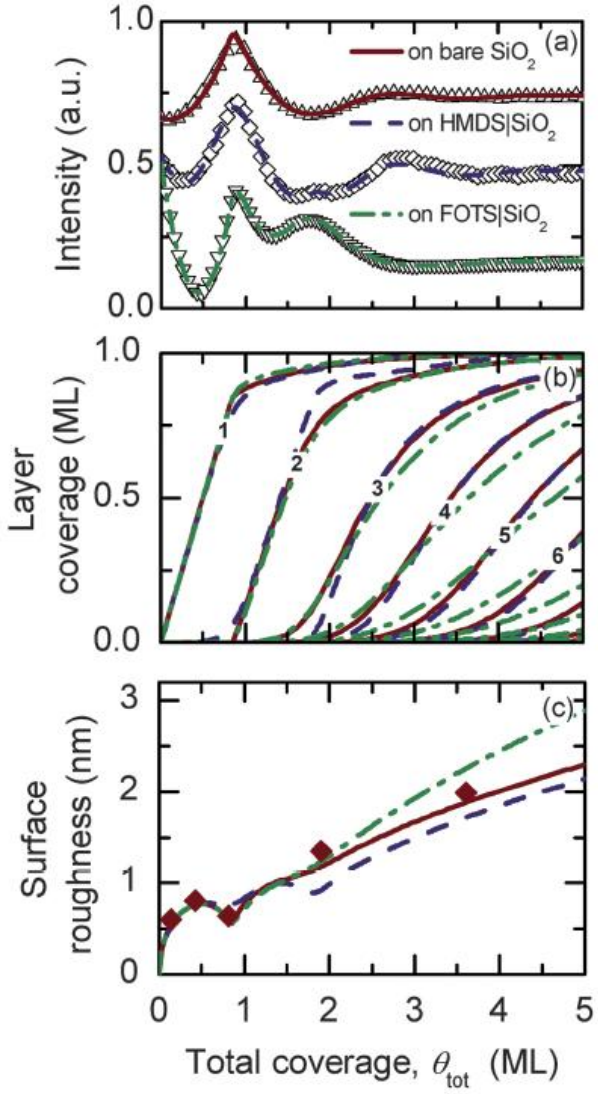


**Figure 3.12.** Anti-Bragg scattering of pentacene growth on $SiO_2$, HMDS treated $SiO_2$, and FOTS treated $SiO_2$. (a) X-ray intensity at the Anti-Bragg position collected *in-situ* and in real-time as a function of deposited material. Line traces show the fits to the growth model. (b) The coverage of individual layers as a function of total deposited coverage. (c) Pentacene surface roughness as calculated from the layer coverages. Solid diamonds show experimentally measured roughness from AFM on $SiO_2$, showing good agreement with the model.

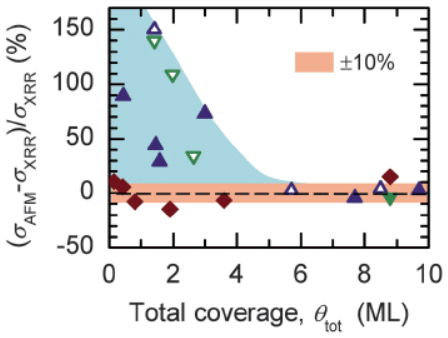


**Figure 3.13.** The error in surface roughness from *ex-situ* AFM measurements, as compared to surface roughness prediction from Anti-Bragg growth model, which we regard is the true value of surface roughness. Diamonds indicate films on $SiO_2$, triangles indicate films on HMDS, and inverted triangles indicate films on FOTS.

The thermodynamic driving force for the formation of pentacene film layer-by-layer versus 3D islands can be assessed using capillary theory by considering this combination of surface energies:

$$\gamma_{(001)} - \gamma_{sub} + \gamma_{int} \qquad (5)$$

where $\gamma_{(001)}$ is the pentacene surface energy, $\gamma_{sub}$ is the substrate surface energy, and $\gamma_{int}$ is the interfacial surface energy between pentacene and the substrate. Values for the first two surface energies are known from contact angle measurements and literature [92, 74] and are tabulated below.

**Table 3.1.** Surface energies of pentacene growth.

| Surface | $\gamma$ ($mJ/m^2$) | $\gamma_{sub} - \gamma_{(001)}$ ($mJ/m^2$) |
|---|---|---|
| $SiO_2$ | 50 - 60 | 2 - 12 |
| HMDS | 36 | − 12 |
| FOTS | 12 | − 36 |
| $Pe_{(001)}$ | 48 | |

By forming a pentacene layer on top the substrate, we replace the surface energy of the substrate with the pentacene surface energy and the energy of the newly created interface. If the substrate energy is lower than the sum of the two other energies, we expect the pentacene layer formation to be unstable on top the substrate. As the interfacial energy is not known, we tabulated the maximum value of the interfacial energy to form the pentacene monolayer, $\gamma_{sub} - \gamma_{(001)}$ , in Table 3.1. While negative interfacial energies have been observed for oil/water interfaces [93], the interfacial energy is typically regarded as a positive quantity. Thus, we see that in the case of pentacene growth on HMDS and FOTS, there is a driving force for dewetting. In the case of $SiO_2$, the monolayer formation will be stable if the interfacial energy is low (2-12 $mJ/m^2$) and our experimental evidence suggest that it is low enough to prevent dewetting.

We observed that exposure of ultra thin pentacene films to ambient air causes significant stabilization of the surface morphology, as the dewetting process appears to halt. A possible explanation of this phenomenon starts with a look at pentacene surface energies at step edges, which are 77-100 $mJ/m^2$ depending on crystallographic orientation [74]. Such surface energies are significantly higher than the previously mentioned surface energies involved in thin film growth. Therefore, it is possible that exposure to ambient air leads to formation of a water layer on the surface of pentacene and the adsorption of molecules at the pentacene step edges and grain boundaries. Alternatively, the pentacene surface could be oxidizing or photo-oxidizing upon exposure to ambient conditions, which would result in formation of hydroxyl and carbonyl groups on pentacene [94]. Since dewetting in pentacene starts from step edges or grain boundaries, the proposed process would stabilize such interfaces and inhibit pentacene “upward” transport.

Molecules located at the step edges of a terrace, an island, a vacancy cluster, or grain boundary (as the triclinic lattice leads to significant mismatch and void formation at the grain boundaries) are the most weakly bound, and so they are prime candidates to undergo "upward" interlayer transport on low-energy surfaces. These molecules could detach or move by overcoming only a fraction of the pentacene bulk cohesion energy of 1.3 eV [92]. This means that "upward" transport is likely thermally activated, thus causing morphological changes to occur faster at elevated temperatures [95]. From AFM of dewetting pentacene on HMDS, we observed formation of pits in the first ML, which seem to initiate the dewetting process and grow in size as dewetting proceeds and more material is moved from the first ML upwards. From Anti-Bragg Scattering analysis, we observed that upon deposition of 5 MLs of pentacene, the first and second MLs are at nearly complete coverage, the third ML is at 90% coverage, the fourth ML is at 80%, and the fifth ML is at 65%, with the sixth and seventh MLs already nucleated. Such complete layer coverage of the interfacial MLs would cause the dewetting initiation sites to be buried and the dewetting processing inhibited. This hypothesis explains the convergence between the roughness values after the deposition of 5 MLs of pentacene.

We have mentioned "upward" transport in explaining dewetting, but "upward" transport was not part of the layer population model used in Anti-Bragg Scattering analysis (Equation 4). The reason for this is that the time scale of pentacene reorganization is much longer as compared to the pentacene deposition, which takes 15-20 sec for 1 ML. In addition, the excellent agreement between the model fit and the measured intensity may suggest that "upward" transport is not important during growth under our experimental conditions.

### *2.4 Conclusion*

We have observed evidence for reorganization of thin pentacene films deposited on HMDS or FOTS treated $SiO_2$, reminiscent of dewetting. In thin films with coverage near a monolayer, these changes resulted in the depletion of the first monolayer via formation of multilayer islands with adjacent pits. Such dewetting occurs in an inert atmosphere (vacuum or nitrogen); however it appears to be quenched upon exposure to ambient air. By combining *in-situ* time-resolved Anti-Bragg Scattering and *ex-situ* AFM, we have conclusively determined the growth mode and morphology of pristine thin films and shown that thin films with thickness of 5 MLs or less are susceptible to reorganization.

## *3. Solvent Annealing*

### *3.1 Pentacene solvent annealing*

Processing of most solution-processed organic semiconductors, includes a post-deposition thermal annealing step in order to promote crystallization and grain growth for OTFTs [96, 97] or to induce phase segregation for OPVs [98, 99]. This method is used due to its simplicity and wide spread use in inorganic processing, but it has significant draw-backs in the case of organic semiconductors. Molecular building blocks tend to be weakly bounded compared to their inorganic counterparts and tend to desorb, dewet, oxidize, or degrade. All of these processes are accelerated at elevated temperatures. In addition, polymer semiconductors tend to undergo melting or phase transitions, which significantly change their properties [49, 51]. Thermal annealing is not material specific and is applied to the entire sample, affecting all of the underlying layers, including the substrate, which should be limited to a processing temperature of 200 °C for flexible substrate, such as polyethylene terephthalate.

Therefore, thermal annealing needs to be performed with significant consideration for all of the constituent film layers and substrates.

An alternative approach to induce structural order in organic materials has been solvent annealing, commonly used to induce nanostructural organization in block-copolymers [100]. Such method is an ideal alternative to thermal annealing for organic semiconductors. Solvent annealing may be performed under inert atmosphere to reduce chemical degradation and without applying a thermal load. In addition, solvent annealing may be tuned to induce changes in a single layer by utilizing polarity or solubility differences.

The effects of solvent vapor annealing have been shown for pentacene [101, 102] and blends of P3HT:PCBM [103]. The complex interactions between the solvent molecules and organic films have not been well understood; in fact, it is quite puzzling why pentacene, insoluble in acetone, reorganizes upon exposure to acetone vapor. In order to get a better understanding of the interaction between solvent and organic film, as well as an insight into the dynamics of the solvent annealing process itself, we carried out *in-situ* GIWAXS and time-resolved optical reflectometry to monitor the acetone solvent vapor annealing of pentacene on $SiO_2$.

### *3.2 In-situ pentacene solvent annealing*

Solvent annealing was carried out in a custom-made chamber [104], consisting of an air tight enclosure with Kapton windows for X-rays. Ultra high purity helium was flown through the enclosure to create an inert atmosphere and control the solvent vapor partial pressure. Solvent vapor was introduced by injecting solvent into the enclosure through a valved inlet. A pentacene thin film (30 nm) deposited on silicon wafer with a 361.2 nm $SiO_2$ layer was used for solvent annealing.

Optical reflectometry measurements were performed *in-situ* and in real-time during solvent annealing using FilMetrics F30 spectrometers (λ = 400nm – 1100nm). The reflectance spectrum is due to the semi-infinite Si substrate, $SiO_2$ layer, and pentacene layers. The position of maxima and minima ($\lambda_{min}$) shift as the optical thickness of the sample changes with solvent uptake and provides information on adsorption or penetration of the solvent in the film.

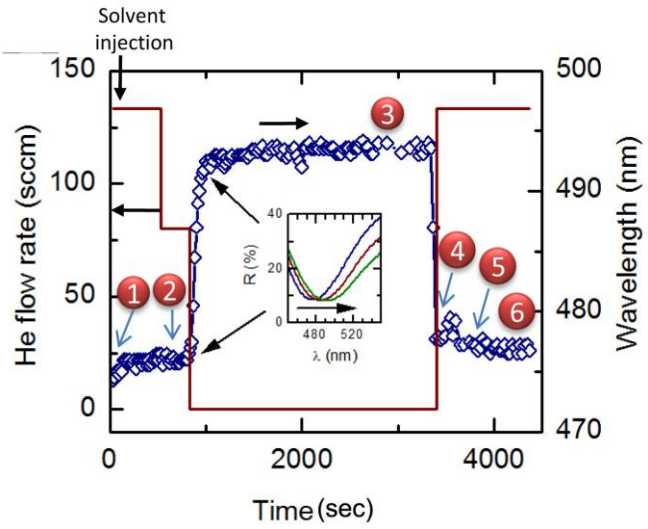


**Figure 3.14.** Optical reflectance of pentacene thin film during solvent annealing. The evolution spectral shift, $\Delta\lambda_{min}$, of the reflectance minimum located at $\Delta\lambda_{min} = 474$ *nm* (inset).

The time evolution of the spectral shift, $\Delta\lambda_{min}$, for the minima located at $\lambda_{min} \approx$ 475 nm is shown in Figure 3.14. The sample is kept under inert atmosphere before the solvent is injected (t = 120 s) with the Helium flow at 130 sccm. Such an elevated flow rate prevents solvent vapor from building up. A small shift, $\Delta\lambda_{min}$ ~ 1-2 nm, is detected after solvent injection indicating that small amounts of acetone adsorb on the surface. In order to allow solvent vapor to build up, helium flow was reduced to

80sccm (t = 600 s) and then to zero (t = 900 s). After the helium flow was turned off, we observed an instantaneous large red-shift in the absorption minima ($\Delta\lambda_{min}$ ~ 16 nm) followed by a further transient shift to $\Delta\lambda_{min}$ ~ 19 nm. After a period of solvent annealing, the Helium flow was restored to 130 sccm and the absorption minima returned instantaneously to $\Delta\lambda_{min}$ ~ 4 nm and gradually shifted further to $\Delta\lambda_{min}$ ~ 2-3 nm. This indicates that most of the solvent was removed from the surface of pentacene immediately with some residual solvent being left behind.

Fitting the reflectance data with a layered optical model [104], produces a conversion between $\Delta\lambda_{min}$ and the change in film thickness, $\Delta t$, to be:

$$\Delta\lambda_{\min}\ 1.0\text{nm} \sim \Delta t\ 1.6\text{nm}$$

Based on this result, we conclude that upon initial injection of solvent into the chamber a ~2.5nm thick acetone layer formed on the surface of pentacene film. When the helium flow was turned off, resulting in maximum solvent vapor pressure, a ~30nm thick acetone layer formed on the surface. The absorption spectra did not show any changes in the vibronic peaks, suggesting that the acetone only adsorbed to the surface and did not swell the pentacene film, as would be expected for solvent annealing. X-ray measurements taken during the solvent annealing would reveal any swelling or disorder due to solvent uptake, as well as the structural reorganization taking place.

In Figure 3.15, we show some of the GIWAXS images taken during various stages of solvent annealing: before solvent annealing (1), after the injection of solvent (2), at maximum solvent vapor saturation (3), after the increase in helium flow to remove the acetone solvent (4), after the solvent has been removed (5,6). From these measurements we observe that pentacene films transform from the initial "thin-film" phase to the bulk phase. These two phases are most easily differentiated by their diffraction peaks along the (11L) rod, as noted in the Figure 3.15 by $TF_{(1-3)}$ and $B_{(1-3)}$

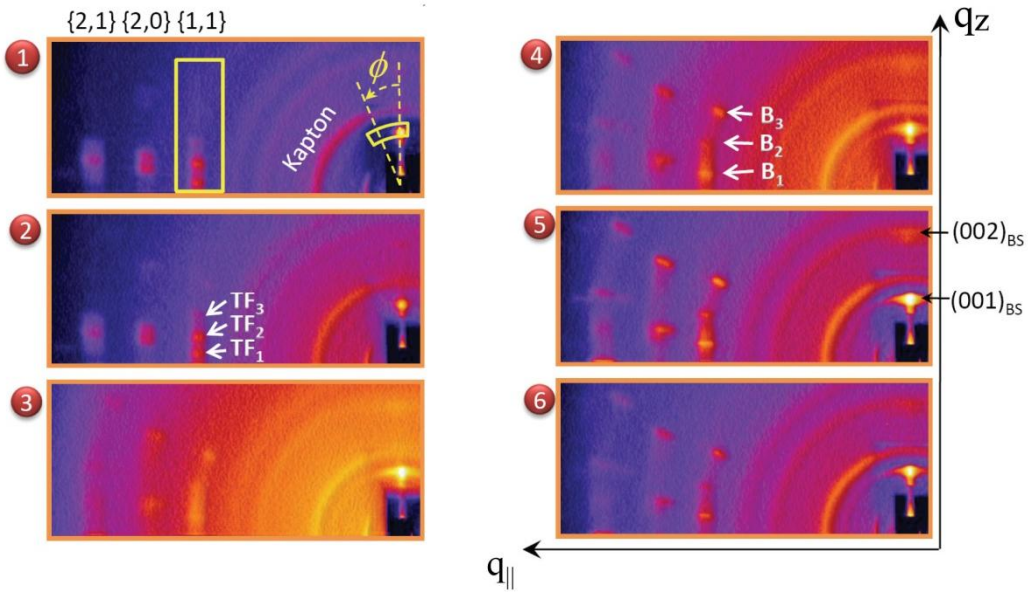


**Figure 3.15.** GIWAXS snapshots of *in-situ* solvent annealing of pentacene. (1) Before any solvent was introduced. (2) Solvent was injected into the cell. (3) Solvent annealing at maximum solvent vapor saturation. (4) Solvent vapor pressure reduced. (5) Most of solvent vapor removed. (6) All of the residual solvent has been removed. $TF_x$ and $B_x$ are characteristic peaks of "thin-film" and bulk phase polymorphs of pentacene, respectively. The radial distribution of the out-of-plane scattering, $\varphi$, indicates the amount of disorder in the film.

for "thin-film" and bulk phase, respectively. In addition, we do not observe significant movement in the diffraction spots, especially in the out-of-plane direction. The degree of disorder in the film is characterized by the radial distribution of the (001) peak ($\varphi$). During the solvent annealing process, we observe that the thin film becomes slightly more disordered and then partially recovers the ordering once the solvent is removed. This indicates that long-range order in the thin film is maintained during the annealing process and no swelling or expansion of the unit cell occurs, as supported by the reflectivity measurement. Therefore, solvent molecules appear to

remain near the film surface and grain boundaries, from where they induce a transition.

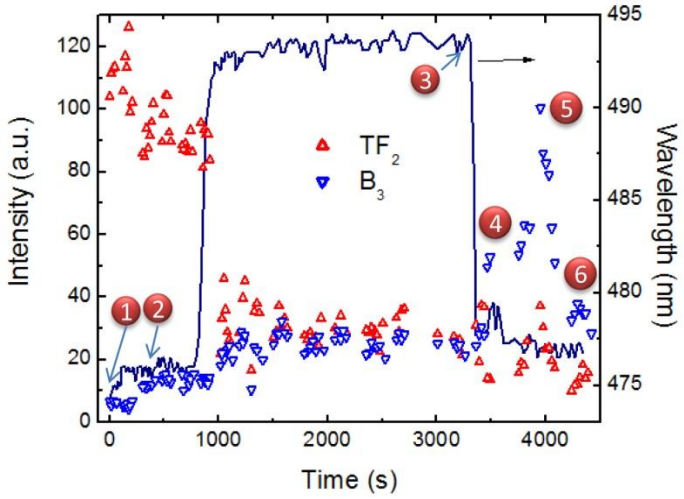


**Figure 3.16.** Time evolution of the integrated peak intensities of the "thin-film" phase, $TF_2$, and bulk phase, $B_3$.during solvent annealing. The $\Delta\lambda_{min}$ is shown to indicate the amount of solvent adsorbed on the pentacene surface. (1) Before any solvent was introduced. (2) Solvent was injected into the cell. (3) Solvent annealing at maximum solvent vapor saturation. (4) Solvent vapor pressure reduced. (5) Most of solvent vapor removed. (6) All of the residual solvent has been removed.

Bulk phase appears in the scattering data immediately after the injection of solvent and as the acetone vapor pressure increases, the bulk phase diffraction spots become more intense, as the diffraction from the "thin-film" phase decreases. This suggests that solvent molecules initiate a solid-to-solid transition from "thin-film" to bulk phase. To show the solvent annealing process more clearly, we combined the reflectivity data, which is indicative of the solvent adsorption to the surface, with the intensities of "thin-film" ($TF_2$) and bulk ($B_3$) phase diffraction peaks in Figure 3.16. The bulk phase starts to form as the solvent is introduced in the chamber and significantly increases with the solvent vapor pressure saturation. This suggests that

bulk phase transformation is limited by the supply of solvent at the film surface. It also suggests that the phase transformation and polymorphism of the thin film can be controlled by tuning the solvent vapor pressure in the annealing chamber. The irreversible increase in disorder in the film from the radial distribution of the (001) peak, may be the result of thin film cracking due to the volume change upon phase transformation, which results in ~6% contraction in the out-of-plane direction and ~2.5% expansion in the in-plane direction.

An interesting behavior is observed in the GIWAXS data, as the solvent is being removed from the chamber (Figure 3.16 (5) ). The scattering intensities increase and then decrease, with bulk phase peak demonstrating a larger increase in intensity than the "thin-film" phase. This behavior is not due to photon flux, as all image intensities are normalized.

### *3.3 Discussion of pentacene solvent annealing*

We have determined that solvent adsorbs to the thin film surface and initiates pentacene phase transformation from "thin-film" to bulk phase. The top surface of pentacene is typically rough due to the 3D growth of films past a few MLs. Combined with rough topography, the volume change from the phase transition would result in bending or cracking of crystallites upon solvent annealing.

The observed transient increase in X-ray diffraction intensity suggests that the film becomes more crystalline and then reverts to a less crystalline state. This scenario may be explained by considering how a solvent propagates inside the film. As the crystallites undergo structural reorganization, cracks open up and allow solvent to move deeper into the film and initiate further structural reorganization. When the solvent is removed from the chamber, some residual solvent would remain trapped within the cracks in the thin film due to capillary forces. The residual solvent does

eventually leave the film, as evidenced by the transient change in film thickness ($\Delta\lambda_{min}$). As the solvent evaporates, it exerts a capillary pull on the facets in the cracks, which pulls the crystallites back together and keeps the surface energy low as internal crystallite surfaces become exposed. This induces more alignment between crystallites, and would increase the coherent X-ray scattering. Nevertheless, the solvent is eventually entirely removed from the film causing a collapse into a more disordered state, as compared to the original film.

### *3.4 Conclusions*

In summary, we investigated the solvent vapor annealing process of a model thin film of pentacene by combining time-resolved optical reflectometry with time-resolved *in-situ* GIWAXS. From optical measurement, we observed the adsorption of solvent molecules on the surface of pentacene, while GIWAXS provided information of structural reorganization. The transformation from "thin-film" phase to bulk phase occurred without swelling and was correlated with surface solvent adsorption, indicating a solid-solid transition. In addition, from *in-situ* GIWAXS data, we observed temporary realignment of crystallites as a result of capillary pull caused by the removal of residual solvent trapped in cracks created by the unit cell volume change of phase transformation.

### *3.5 Solvent annealing of TIPS-pentacene*

In the previous section, we discussed the dynamics and the potential for solvent annealing to replace thermal annealing as a post-deposition step for inducing order and crystallinity in the organic thin film. The results of pentacene solvent annealing do not show clear advantages of solvent annealing due to cracking caused by the volume change of the unit cell upon phase transformation. In this section, we

demonstrate the advantage of solvent annealing over thermal annealing for a solution-processable pentacene derivative.

Pentacene has been an excellent model material for organic electronics, but the insoluble nature has been a major drawback, as one of the proposed advantages of organics is the ease of processing. In recent years, pentacene derivatives have been synthesized with functional silyl groups, like 6,13-bis(triisopropyl-silylethynyl) pentacene (TIPS-pentacene), in order to facilitate dissolution (see Figure 3.17 for structure). This material has shown excellent crystallinity and field-effect mobility, in excess of 1 $cm^2$/Vs upon drop casting from solution [105]. In addition, TIPS-pentacene has been combined with buckminsterfullerene in heterojunction solar cells and achieved a power conversion efficiency of 0.52% [106]. This result was achieved after thermal annealing at 265 °C and addition of mobile ions to improve charge extraction. Thermal annealing achieved improved crystallinity of the TIPS-pentacene layer, but such high temperatures are not compatible with flexible substrates and significantly limit the choice of the materials for the solar cell. In order to show the capabilities of solvent annealing, we compare the effects of solvent and thermal annealing of TIPS-pentacene films.

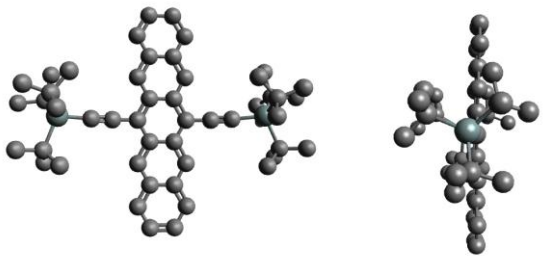

**Figure 3.17.** Structure of TIPS-pentacene.

TIPS-pentacene was obtained from Dr. John Anthony from University of Kentucky. Toluene was added to crystals of TIPS-pentacene to form solutions of 20 mg/ml. Solutions were stirred for a minimum of one hour and filtered (0.2μm) before

forming thin films. Thin films were spin coated on soda lime glass and $SiO_2$ substrates. Solvent annealing was performed inside a solvent annealing chamber, described in the earlier section, using toluene. GIWAXS measurements were carried out at D1 beamline at CHESS. Additionally, a Scintag diffractometer was used to take a $\theta$-$2\theta$ scan of thin films before and after annealing. Topography of the thin films was studied using DI-3100 Dimension microscope in tapping mode.

Gathered GIWAXS images of scattering from as-spun and solvent annealed thin films of TIPS-pentacene are shown in Figure 3.18. Broad scattering intensities in the as-spun diffraction pattern show diffuse scattering rings characteristic of a randomly oriented film. The solvent annealed sample, on the other hand, shows much better defined scattering pattern with significant in-plane crystallinity as evidenced by the many orders of diffraction peaks along the crystal truncation rod. In addition, the mosaicity of the out-plane scattering was significantly reduced.

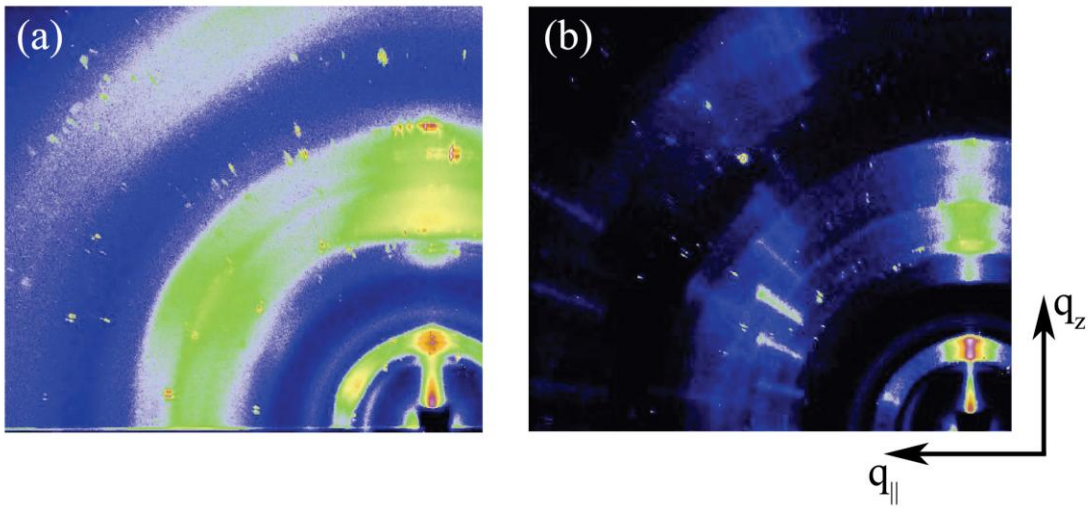


**Figure 3.18.** GIWAXS of as-spun (a) and solvent annealed (b) TIPS-pentacene on soda-lime glass. Wide scattering rings for as-spun thin film indicates a high degree of disorder in the film, whereas formation of crystal truncation rod and well defined scattering for solvent annealed thin film indicated a high degree of crystallinity.

Topography of as spun and solvent annealed samples is shown in Figure 3.19. The as spun sample does not show any crystalline ordering and looks nearly amorphous, as expected from the GIWAXS result. The solvent annealed sample, on the other hand, clearly shows small crystallite formation, which would lead to well-defined diffraction spots. Based on the GIWAXS and AFM results, we observe a significant improvement in the ordering of TIPS-pentacene upon solvent annealing.

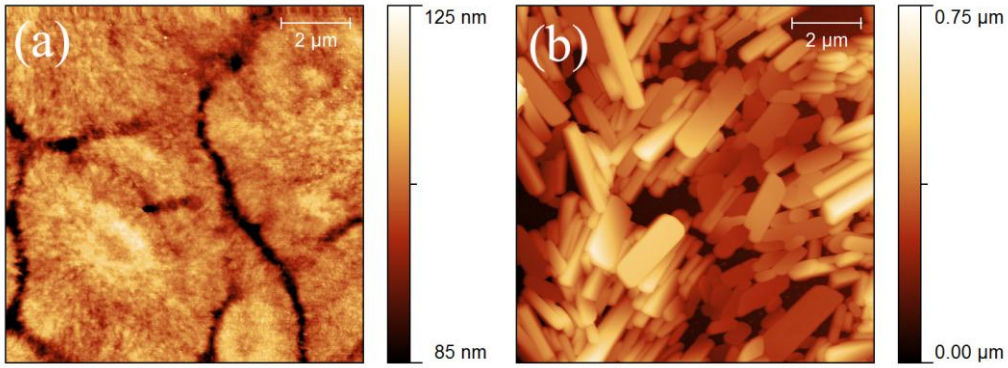


**Figure 3.19.** 10 µm × 10 µm AFM images of as-spun (a) and solvent annealed (b) TIPS-pentacene on soda-lime glass.

In order to compare the quality of thermally annealed films to solvent annealed films, we carried out X-ray diffraction on thin films of TIPS-pentacene on $SiO_2$, as shown in Figure 3.20. We observe that the diffracted intensity is higher in the case of the solvent annealed samples, indicating an enhancement of the crystal structure. In addition, solvent annealed samples show additional diffraction peaks not present in the thermally annealed peaks, suggesting further improvement in the crystal structure.

We have shown significant ordering of TIPS-pentacene upon solvent annealing as compared to as-spun films. In addition, we demonstrated an improvement in crystal structure of solvent annealed film over thermally annealed film, showing great potential for future use of solvent annealing.

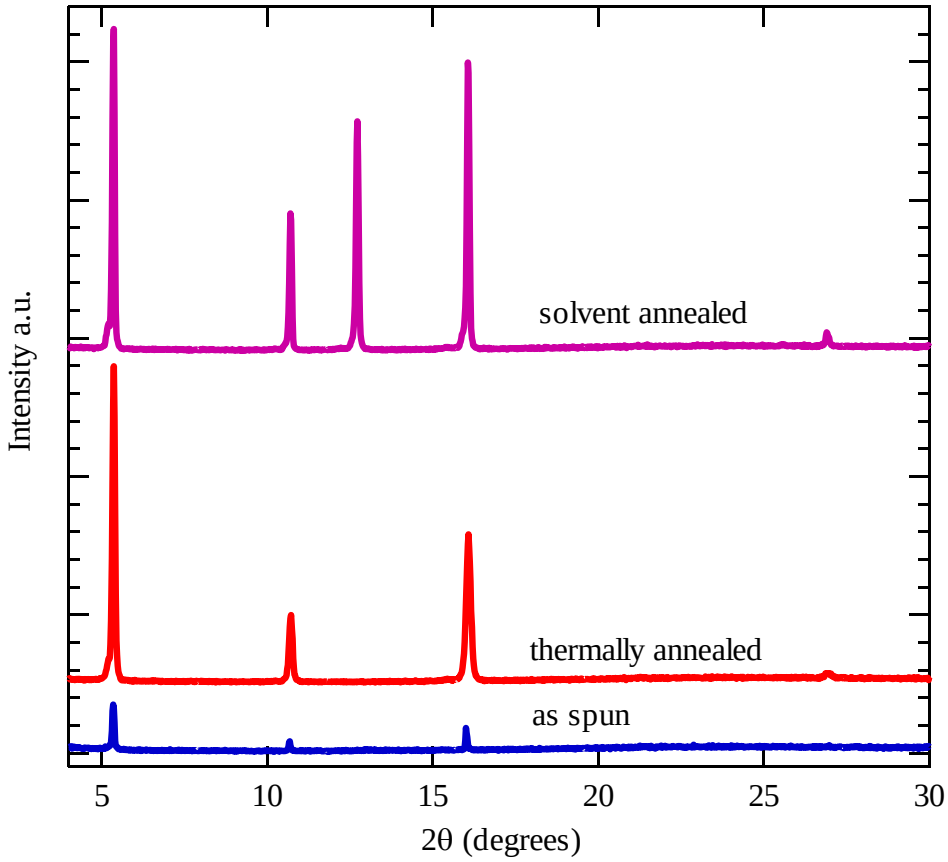


**Figure 3.20.** XRD of as-spun, thermally annealed at 265 °C, and solvent annealed TIPS-pentacene films on $SiO_2$.

# CHAPTER 4

# OUTLOOK ON ORGANIC SEMICONDUCTORS

Organic semiconductors have come a long way since the work described in this dissertation started five years ago. The performance of polymeric materials has significantly improved and these materials are now suitable for commercial applications. Field-effect mobilities approaching 1 $cm^2/Vs$ have been achieved for p-type, n-type, and ambipolar polymers. The next major challenge to be overcome for commercialization of polymeric semiconductors is scalable processing. This step is not easily realized by academic researchers and significant collaboration with industry is required, which will be aided by the completion of numerous AMOLED factories within the next two years.

The development of organic semiconductors has been impressive, but much of the work has been of combinatorial nature and resulted in little new scientific knowledge or understanding of organics. In polymeric semiconductors, the analogy of rigid rod polymers with flexible side-chains, thoroughly studied a decade ago, to the popular polythiophenes has been ignored and as a result, many analytical tools and understanding of polymer behavior has been overlooked.

Much of the recent work in molecular semiconductors has shown that single-grain field-effect transistors yield mobilities well above 1 $cm^2/Vs$, which are necessary for electronic circuits. Unfortunately, the most common growth method used to produce single crystal films is physical vapor deposition, which is not an efficient use of material or very scalable for mass production. An alternative approach to single grain mobility measurements is achieved by the reduction of the electrode dimensions, but that produces a small yield since it depends on the chance alignment of single grains in polycrystalline films from thermal deposition. I have recently demonstrate

an alternative and more robust method of achieving registration between grains of organic semiconductor and contact electrodes by patterning step edges on the substrate prior to organic layer deposition using self assembled monolayers. Step edges created by the self assembled monolayers present a low energy nucleation site for organic material and result in preferential nucleation of pentacene grains along the patterned step edges. Such control over grain position is necessary for fundamental study of charge trapping in grains and grain boundaries and for fabrication of reproducible electronic circuits. In addition, such patterning can be easily achieved by one step patterning of self assembled monolayers with vacuum UV, as was demonstrated more than 20 years ago.

The big challenge to organic electronics is silicon ink. In the past year, Innovalight has achieved a solar cell efficiency of 19% using silicon ink, while the organic solar cell efficiency record is 8.3% by Konarko. Such development of silicon ink challenges organics in ease of processing, as both can be solution processed. I think that silicon ink is still much more expensive as compared to organic materials, but the future of the material of choice for solar cells is still to be discovered.

## REFERENCES


[1] C. TANG and S. VANSLYKE, *Appl. Phys. Lett.* **51**, 913 (1987).

[2] J. BURROUGHES, D. BRADLEY, A. BROWN, R. MARKS, K. MACKAY, R. FRIEND, P. BURNS, and A. HOLMES, *Nature* **347**, 539 (1990).

[3] F. EBISAWA, T. KUROKAWA, and S. NARA, *J. Appl. Phys.* **54**, 3255 (1983).

[4] K. KUDO, M. YAMASHINA, and T. MPRIIZUMI, *Jpn. J. Ap. Phys.* **23**, 130 (1984).

[5] A. TSUMURA, H. KOEZUKA, and T. ANDO, *Appl. Phys. Lett.* **49**, 1210 (1986).

[6] S. ALLARD, M. FORSTER, B. SOUHARCE, H. THIEM, and U. SCHERF, *Angew. Chem., Int. Ed.* **47**, 4070 (2008).

[7] Z. BAO, *Adv. Mater.* **12**, 227+ (2000).

[8] Z. BAO, J. ROGERS, and H. KATZ, *J. Mater. Chem.* **9**, 1895 (1999).

[9] M. M. LING and Z. BAO, *Chem. Mater.* **16**, 4824 (2004).

[10] G. LEISING, B. STADLOBER, U. HAAS, A. HAASE, C. PALFINGER, H. GOLD, and G. JAKOPIC, *Microelectronic Engineering* **83**, 831 (2006), Micro- and Nano-Engineering MNE 2005.

[11] J. ZHANG, C. M. LI, M. B. CHAN-PARK, Q. ZHOU, Y. GAN, F. QIN, B. ONG, and T. CHEN, *Appl. Phys. Lett.* **90** (2007).

[12] J. KY, G. MILLER, and R. ELSENBAUMER, *J. Chem. Soc., Chem. Comm.* , 1346 (1986).

[13] M. SATO, S. TANAKA, and K. KAERIYAMA, *J. Chem. Soc., Chem. Commun.* , 873 (1986).

[14] R. MCCULLOUGH, R. LOWE, M. JAYARAMAN, and D. ANDERSON, *J. Org. Chem.* **58**, 904 (1993).

[15] B. S. ONG, Y. WU, P. LIU, and S. GARDNER, *J. Am. Chem. Soc.* **126**, 3378 (2004).

[16] I. McCulloch, M. Heeney, C. Bailey, K. Genevicius, I. Macdonald, M. Shkunov, D. Sparrowe, S. Tierney, R. Wagner, W. Zhang, M. Chabinyc, R. Kline, M. Mcgehee, and M. Toney, *Nature Mater.* **5**, 328 (2006).

[17] H. E. Katz and J. Huang, *Annu. Rev. Mater. Res.* **39**, 71 (2009).

[18] M. He and F. Zhang, *J. of Org. Chem.* **72**, 442 (2007).

[19] H. H. Fong, V. A. Pozdin, A. Amassian, G. G. Malliaras, D.-M. Smilgies, M. He, S. Gasper, F. Zhang, and M. Sorensen, *J. of Am. Chem. Soc.* **130**, 13202 (2008).

[20] M. He, J. Li, M. L. Sorensen, F. Zhang, R. R. Hancock, H. H. Fong, V. A. Pozdin, D.-M. Smilgies, and G. G. Malliaras, *J. of Am. Chem. Soc.* **131**, 11930 (2009).

[21] M. He, J. Li, A. Tandia, M. Sorensen, F. Zhang, H. H. Fong, V. A. Pozdin, D.-M. Smilgies, and G. G. Malliaras, *Chem. Mat.* **22**, 2770 (2010).

[22] D. Pozdin V.A., Smilgies, *J. Am. Chem. Soc.* (2011), Submitted.

[23] P. Busch, M. Rauscher, D. Smilgies, D. Posselt, and C. Papadakis, *J. of Appl. Crystal.* **39**, 433 (2006).

[24] D.-M. Smilgies, *J. of Appl. Crystal.* **42**, 1030 (2009).

[25] J. L. Baker, L. H. Jimison, S. Mannsfeld, S. Volkman, S. Yin, V. Subramanian, A. Salleo, A. P. Alivisatos, and M. F. Toney, *Langmuir* **26**, 9146 (2010).

[26] D.-M. Smilgies and D. R. Blasini, *J. Appl. Crystallogr.* **40**, 716 (2007).

[27] M. L. Chabinyc, M. F. Toney, R. J. Kline, I. McCulloch, and M. Heeney, *J. of Am. Chem. Soc.* **129**, 3226 (2007).

[28] D. W. Breiby, O. Bunk, J. W. Andreasen, H. T. Lemke, and M. M. Nielsen, *J. of Appl. Crystal.* **41**, 262 (2008).

[29] I. KYMISSIS, *Organic Field Effect Transistors: Theory, Fabrication and Characterization*, Springer, New York, 2009.

[30] L. CHUA, J. ZAUMSEIL, J. CHANG, E. OU, P. HO, H. SIRRINGHAUS, and R. FRIEND, *Nature* **434**, 194 (2005).

[31] C. Y. KAO, B. LEE, L. S. WIELUNSKI, M. HEENEY, I. MCCULLOCH, E. GARFUNKEL, L. C. FELDMAN, and V. PODZOROV, *Adv. Funct. Mater.* **19**, 1906 (2009).

[32] D. A. LYASHENKO, A. A. ZAKHIDOV, V. A. POZDIN, and G. G. MALLIARAS, *Org. Electron.* **11**, 1507 (2010).

[33] G. HOROWITZ, *Adv. Mater.* **10**, 365 (1998).

[34] D. M. DELONGCHAMP, R. J. KLINE, E. K. LIN, D. A. FISCHER, L. J. RICHTER, L. A. LUCAS, M. HEENEY, I. MCCULLOCH, and J. E. NORTHRUP, *Adv. Mat.* **19**, 833+ (2007).

[35] R. AZUMI, E. MENA-OSTERITZ, R. BOESE, J. BENET-BUCHHOLZ, and P. BAUERLE, *J. Mater. Chem.* **16**, 728 (2006).

[36] J. E. NORTHRUP, *Phys. Rev. B* **76** (2007).

[37] I. MCCULLOCH, M. HEENEY, M. L. CHABINYC, D. DELONGCHAMP, R. J. KLINE, M. COELLE, W. DUFFY, D. FISCHER, D. GUNDLACH, B. HAMADANI, R. HAMILTON, L. RICHTER, A. SALLEO, M. SHKUNOV, D. SPORROWE, S. TIERNEY, and W. ZHONG, *Adv. Mater.* **21**, 1091 (2009).

[38] R. J. KLINE, D. M. DELONGCHAMP, D. A. FISCHER, E. K. LIN, L. J. RICHTER, M. L. CHABINYC, M. F. TONEY, M. HEENEY, and I. MCCULLOCH, *Macromolecules* **40**, 7960 (2007).

[39] I. OSAKA, R. ZHANG, G. SAUVE, D.-M. SMILGIES, T. KOWALEWSKI, and R. D. MCCULLOUGH, *J. of Am. Chem. Soc.* **131**, 2521 (2009).

[40] I. OSAKA, T. ABE, S. SHINAMURA, E. MIYAZAKI, and K. TAKIMIYA, *J. Am. Chem. Soc.* **132**, 5000 (2010), PMID: 20297819.

[41] H. YAN, Z. CHEN, Y. ZHENG, C. NEWMAN, J. R. QUINN, F. DOTZ, M. KASTLER, and A. FACCHETTI, *Nature* **457**, 679 (2009).

[42] M. HEENEY, C. BAILEY, K. GENEVICIUS, M. SHKUNOV, D. SPARROWE, S. TIERNEY, and I. MCCULLOCH, *J. Am. Chem. Soc.* **127**, 1078 (2005).

[43] H. SIRRINGHAUS, R. WILSON, R. FRIEND, M. INBASEKARAN, W. WU, E. WOO, M. GRELL, and D. BRADLEY, *Appl. Phys. Lett.* **77**, 406 (2000).

[44] P. SONAR, S. P. SINGH, Y. LI, M. S. SOH, and A. DODABALAPUR, *Adv. Mater.* **22**, 5409+ (2010).

[45] J.-F. CHANG, B. SUN, D. W. BREIBY, M. M. NIELSEN, T. I. SÃ¶LLING, M. GILES, I. MCCULLOCH, and H. SIRRINGHAUS, *Chem. Mater.* **16**, 4772 (2004).

[46] D. M. DELONGCHAMP, B. M. VOGEL, Y. JUNG, M. C. GURAU, C. A. RICHTER, O. A. KIRILLOV, J. OBRZUT, D. A. FISCHER, S. SAMBASIVAN, L. J. RICHTER, and E. K. LIN, *Chem. Mater.* **17**, 5610 (2005).

[47] M. WINOKUR, D. SPIEGEL, Y. KIM, S. HOTTA, and A. HEEGER, *Synth. Met.* **28**, C419 (1989).

[48] A. GREINER, H. MARTELOCK, A. NOLL, N. SIEGFRIED, and W. HEITZ, *Polymer* **32**, 1857 (1991), Speciality Polymers '90 Conference.

[49] Z. CHEN, H. LEMKE, S. ALBERT-SEIFRIED, M. CAIRONI, M. M. NIELSEN, M. HEENEY, W. ZHANG, I. MCCULLOCH, and H. SIRRINGHAUS, *Adv. Mater.* **22**, 2371 (2010).

[50] D.-M. SMILGIES, WAXS / GIWAXS @ D1: Conversions.

[51] M. L. CHABINYC, *Polym. Rev.* **48**, 463 (2008).

[52] H. SHI, Y. ZHAO, X. ZHANG, Y. ZHOU, Y. XU, S. ZHOU, D. WANG, C. C. HAN, and D. XU, *Polymer* **45**, 6299 (2004).

[53] S. PRASAD, Z. JIANG, S. K. SINHA, and A. DHINOJWALA, *Phys. Rev. Lett.* **101** (2008).

[54] R. STERN, M. BALLAUFF, G. LIESER, and G. WEGNER, *Polymer* **32**, 2096 (1991).

[55] R. C. SCHULZ, *Pure Appl. Chem.* **56**, 417 (1984).

[56] M. Y. PAIK, J. K. BOSWORTH, D.-M. SMILGIES, E. L. SCHWARTZ, X. ANDRE, and C. K. OBER, *Macromolecules* **43**, 4253 (2010).

[57] B. S. ONG, Y. WU, Y. LI, P. LIU, and H. PAN, *Chem. A Eur. J.* **14**, 4766 (2008).

[58] I. OSAKA, G. SAUVE, R. ZHANG, T. KOWALEWSKI, and R. MCCULLOUGH, *Adv. Mater.* **19**, 4160 (2007).

[59] A. FINNEFROCK, R. ULRICH, G. TOOMBES, S. GRUNER, and U. WIESNER, *J. of Am. Chem. Soc.* **125**, 13084 (2003).

[60] R. ALBALAK, E. THOMAS, and M. CAPEL, *Polymer* **38**, 3819 (1997).

[61] R. DURAN, M. BALLAUFF, M. WENZEL, and G. WEGNER, *Macromolecules* **21**, 2897 (1988).

[62] K. TASHIRA, K. ONO, Y. MINAGAWA, M. KOBAYASHI, T. KAWAI, and K. YOSHINO, *J. Polym. Sci., Polym Ed* **29**, 1223 (1991).

[63] K. GAUTAM and A. DHINOJWALA, *Phys. Rev. Lett.* **88** (2002).

[64] S.-A. CHEN and S.-J. LEE, *Synth. Met.* **72**, 253 (1995).

[65] T. AHN, H. J. SUK, J. WON, and M. H. YI, *Microelectron. Eng.* **86**, 41 (2009).

[66] H. N. LEE, Y. G. LEE, I. H. KO, E. C. HWANG, and S. K. KANG, *Curr. App. Phys.* **8**, 626 (2008).

[67] S. NAM, J. JANG, K. KIM, W. M. YUN, D. S. CHUNG, J. HWANG, O. K. KWON, T. CHANG, and C. E. PARK, *J. Mater. Chem.* **21**, 775 (2011).

[68] X.-H. ZHANG, B. DOMERCQ, X. WANG, S. YOO, T. KONDO, Z. L. WANG, and B. KIPPELEN, *Org. Electron.* **8**, 718 (2007).

[69] R. RUIZ, A. MAYER, G. MALLIARAS, B. NICKEL, G. SCOLES, A. KAZIMIROV, H. KIM, R. HEADRICK, and Z. ISLAM, *Appl. Phys. Lett.* **85**, 4926 (2004).

[70] C. DIMITRAKOPOULOS, A. BROWN, and A. POMP, *J. Appl. Phys.* **80**, 2501 (1996).

[71] T. J. CAMPBELL, RB and M. J, *Acta Cryst.* **15**, 289 (1962).

[72] S. KOWARIK, A. GERLACH, S. SELLNER, F. SCHREIBER, L. CAVALCANTI, and O. KONOVALOV, *Phys. Rev. Lett.* **96** (2006).

[73] S. KOWARIK, A. GERLACH, M. W. A. SKODA, S. SELLNER, and F. SCHREIBER, *Eur. Phys. J. - Spec. Top.* **167**, 11 (2009).

[74] S. VERLAAK, S. STEUDEL, P. HEREMANS, D. JANSSEN, and M. DELEUZE, *Phys. Rev. B* **68** (2003).

[75] Y. SUN, Y. LIU, and D. ZHU, *J. Mater. Chem.* **15**, 53 (2005).

[76] R. RUIZ, A. PAPADIMITRATOS, A. MAYER, and G. MALLIARAS, *Adv. Mater.* **17**, 1795+ (2005).

[77] C. DIMITRAKOPOULOS and P. MALENFANT, *Adv. Mater.* **14**, 99+ (2002).

[78] E. GRANSTROM and C. FRISBIE, *J. Phys. Chem. B* **103**, 8842 (1999).

[79] M. FIEBIG, D. BECKMEIER, and B. NICKEL, *Appl. Phys. Lett.* **96** (2010).

[80] T. KELLEY, L. BOARDMAN, T. DUNBAR, D. MUYRES, M. PELLERITE, and T. SMITH, *J. Phys. Chem. B* **107**, 5877 (2003).

[81] H. YANG, T. SHIN, M. LING, K. CHO, C. RYU, and Z. BAO, *J. Am. Chem. Soc.* **127**, 11542 (2005).

[82] J. KANG and X. ZHU, *Appl. Phys. Lett.* **82**, 3248 (2003).

[83] G. BEERNINK, T. STRUNSKUS, G. WITTE, and C. WOLL, *Appl. Phys. Lett.* **85**, 398 (2004).

[84] A. KILLAMPALLI and J. ENGSTROM, *Appl. Phys. Lett.* **88** (2006).

[85] D. KAELBLE, *J. Adhes.* **2**, 66 (1970).

[86] D. DALE, Y. SUZUKI, and J. D. BROCK, *J. Phys.: Condens. Matter* **20** (2008).

[87] A. MAYER, R. RUIZ, H. ZHOU, R. HEADRICK, A. KAZIMIROV, and G. MALLIARAS, *Phys. Rev. B* **73** (2006).

[88] J. ALS-NIELSEN and D. MCMORROW, *Elements of Modern X-ray Physics*, Wiley, New York, 2001.

[89] P. COHEN, G. PETRICH, P. PUKITE, G. WHALEY, and A. ARROTT, *Surf. Sci.* **216**, 222 (1989).

[90] S. HONG, A. AMASSIAN, A. R. WOLL, S. BHARGAVA, J. D. FERGUSON, G. G. MALLIARAS, J. D. BROCK, and J. R. ENGSTROM, *Appl. Phys. Lett.* **92** (2008).

[91] A. C. MAYER, R. RUIZ, R. L. HEADRICK, A. KAZIMIROV, and G. G. MALLIARAS, *Org. Electron.* **5**, 257 (2004).

[92] J. NORTHRUP, M. TIAGO, and S. LOUIE, *Phys. Rev. B* **66** (2002).

[93] L. PRINCE, *J. Colloid Interface Sci.* **23**, 165 (1967).

[94] H. YANG, L. YANG, M.-M. LING, S. LASTELLA, D. D. GANDHI, G. RAMANATH, Z. BAO, and C. V. RYU, *J. Phys. Chem. C* **112**, 16161 (2008).

[95] D. KAFER, C. WOLL, and G. WITTE, *Appl. Phys. A* **95**, 273 (2009).

[96] R. BEN CHAABANE, A. LTAIEF, C. DRIDI, H. RAHMOUNI, A. BOUAZIZI, and H. BEN OUADA, *Thin Solid Films* **427**, 371 (2003).

[97] T. AHN, H. JUNG, H. J. SUK, and M. H. YI, *Synth. Met.* **159**, 1277 (2009).

[98] G. LI, V. SHROTRIYA, J. HUANG, Y. YAO, T. MORIARTY, K. EMERY, and Y. YANG, *Nat. Mater.* **4**, 864 (2005).

[99] T. M. CLARKE, A. M. BALLANTYNE, J. NELSON, D. D. C. BRADLEY, and J. R. DURRANT, *Adv. Funct. Mater.* **18**, 4029 (2008).

[100] J. K. BOSWORTH, M. Y. PAIK, R. RUIZ, E. L. SCHWARTZ, J. Q. HUANG, A. W. KO, D.-M. SMILGIES, C. T. BLACK, and C. K. OBER, *ACS Nano* **2**, 1396 (2008).

[101] D. GUNDLACH, T. JACKSON, D. SCHLOM, and S. NELSON, *Appl. Phys. Lett.* **74**, 3302 (1999).

[102] H. YOSHIDA and N. SATO, *Appl. Phys. Lett.* **89** (2006).

[103] S. MILLER, G. FANCHINI, Y.-Y. LIN, C. LI, C.-W. CHEN, W.-F. SU, and M. CHHOWALLA, *J. Mater. Chem.* **18**, 306 (2008).

[104] A. AMASSIAN, V. A. POZDIN, R. LI, D.-M. SMILGIES, and G. G. MALLIARAS, *J. Mater. Chem.* **20**, 2623 (2010).

[105] S. K. PARK, T. N. JACKSON, J. E. ANTHONY, and D. A. MOUREY, *Appl. Phys. Lett.* **91** (2007).

[106] M. T. LLOYD, A. C. MAYER, A. S. TAYI, A. M. BOWEN, T. G. KASEN, D. J. HERMAN, D. A. MOUREY, J. E. ANTHONY, and G. G. MALLIARAS, *Org. Electron.* **7**, 243 (2006).

LIST OF EQUATIONS